UNIVERSITY OF PADUA

Master degree in Electronic Engineering

Axial Flux Motor

Design optimization by means of copper additive manufacturing

Candidate

Pietro Alessio

Supervisor

Prof. Nicola Bianchi

Date: 07/07/2025

Academic Year 2024/2025

Contents

Abstract

(ENG) This thesis presents the design and analysis of a yokeless axial flux electric motor, leveraging the unique advantages of pure copper additive manufacturing. By exploiting the enhanced geometric freedom and improved material utilization offered by advanced 3D printing technologies, a novel motor architecture is developed with a strong focus on performance optimization and loss reduction. The absence of a central magnetic yoke not only simplifies the magnetic path but also enables a more compact and lightweight configuration. Detailed electromagnetic modeling, thermal analysis, and analytical loss evaluations are conducted to validate the proposed design. The outcome highlights the transformative potential of additive manufacturing in electric motor development, enabling breakthroughs in both performance and design flexibility.

(ITA) Questa tesi presenta la progettazione e l'analisi di un motore elettrico a flusso assiale senza yoke, sfruttando i vantaggi unici offerti dalla manifattura additiva in rame puro. Utilizzando la maggiore libertà geometrica e il miglior utilizzo del materiale resi possibili dalle tecnologie avanzate di stampa 3D, è stata sviluppata una nuova architettura di motore con un forte focus sull'ottimizzazione delle prestazioni e sulla riduzione delle perdite. L'assenza del nucleo magnetico centrale semplifica il percorso del flusso magnetico e consente una configurazione più compatta e leggera. Sono stati condotti modellazioni elettromagnetiche dettagliate, analisi termiche e valutazioni analitiche delle perdite per validare il progetto. Il lavoro evidenzia il potenziale trasformativo della manifattura additiva nello sviluppo di motori elettrici, aprendo la strada a nuovi traguardi in termini di prestazioni e flessibilità progettuale.

List of Symbols

Symbol	**Unit**	**Description**	**Expression**
$2P$	–	number of poles	–
P	–	number of pole pairs	$\frac{2P}{2}$
f_{el}	Hz	electrical frequency	–
n	RPM	mechanical speed	$\frac{60 \cdot f_{el}}{P}$
ω_{el}	rad/s	electrical angular speed	$2\pi \cdot f_{el}$
ω_m	rad/s	mechanical angular speed	$\frac{2\pi}{60} \cdot n$
T_{el}	s	electrical period	$\frac{1}{f_{el}}$
μ_0	H/m	vacuum magnetic permeability	$4\pi \times 10^{-7}$
μ_r	–	relative magnetic permeability	depends on material (B-H curve)
H	A/m	magnetic field intensity	–
B	T	magnetic flux density	$B = \mu_0 \mu_r H$
Λ	Vs	magnetic flux	$\Lambda = \int_S \vec{B} \cdot d\vec{A}$

Mechanical and electromagnetic symbols used throughout the thesis

Symbol	**Unit**	**Description**	**Expression**
ρ	$\Omega \cdot m$	electrical resistivity	–
σ	S/m	electrical conductivity	$\sigma = \frac{1}{\rho}$
α	K^{-1}	temperature coefficient of resistivity	–
κ	W/(m·K)	thermal conductivity	–
L	$W \cdot \Omega / K^2$	Lorenz number (Wiedemann–Franz Law)	$\approx 2.45 \times 10^{-8}$

Material parameters used throughout the thesis

List of Figures

List of Tables

1. Yokeless axial flux motor

1 Introduction

The yokeless axial flux motor represents a significant advancement in electric machine design, particularly suited for applications demanding high power and torque densities, such as electric vehicles, aerospace systems, and advanced energy generation. This architecture is defined by two distinctive features: the elimination of the magnetic yoke in the stator and the use of a segmented armature composed of independent modular units. These structural innovations have important consequences from electromagnetic, mechanical, and thermal perspectives, directly influencing the motor's performance, loss distribution, and manufacturability.

Among the key advantages of yokeless axial flux machines is the potential to employ multiple active air gaps, thereby enabling highly compact and torque-dense configurations. One such topology is the double rotor axial flux motor (DRAFM), in which two rotors are arranged coaxially on either side of a centrally mounted stator. Each rotor carries a set of axially magnetized permanent magnets distributed evenly along a circular path, establishing a closed magnetic circuit that passes axially through the stator.

Unlike conventional radial flux machines, axial flux topologies inherently offer shorter magnetic path lengths and reduced magnetic reluctance. In the yokeless configuration specifically, the stator lacks a traditional ferromagnetic back iron: magnetic flux generated by the rotor magnets is confined and redirected directly between opposing rotors through the stator teeth. This results in a compact and efficient magnetic path, minimizing the use of magnetic material and significantly lowering core losses, particularly those associated with hysteresis and eddy currents. The absence of the yoke also contributes to a lighter machine and frees up valuable space that can be used to increase the copper fill factor of the windings, enabling higher current densities and improved torque output.

The stator is composed of modular segments, each integrating a concentrated copper winding and a ferromagnetic tooth. This segmentation simplifies manufacturing and maintenance operations, and allows for targeted thermal management strategies, an important benefit for motors operating under high current and elevated temperature conditions.

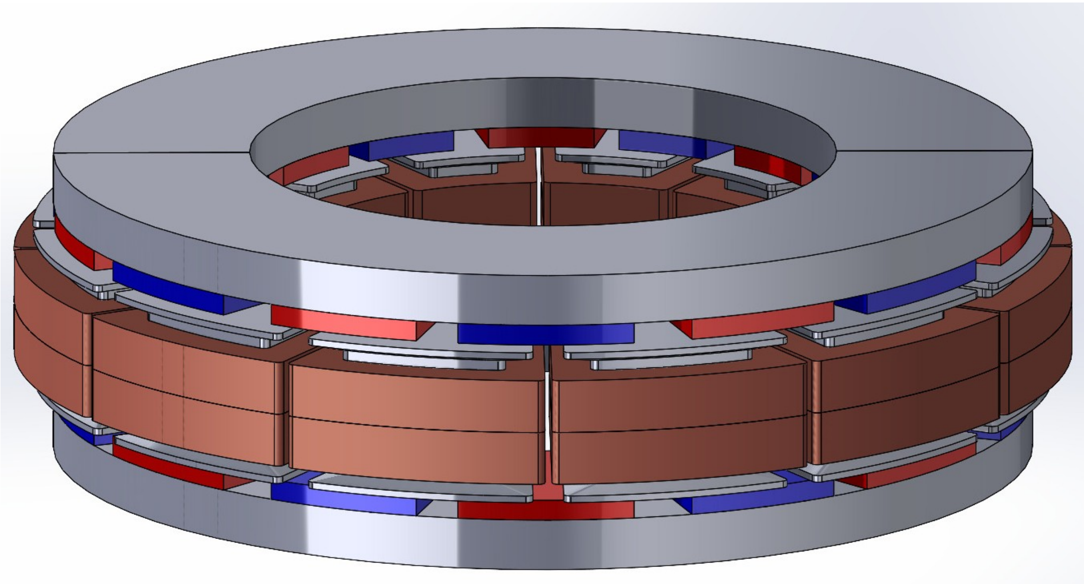

Figure 1.1: Double rotor axial flux motor

Despite these advantages, the DRAFM configuration also presents specific engineering challenges. The strong magnetic attraction between the opposing rotors tends to induce deflection in the rotor back irons, where the magnets are mounted. While this deformation is usually small, it must be tightly controlled, as even slight reductions in the air gap can lead to mechanical contact between rotors and stator. Such contact would result in catastrophic failure of the machine. Moreover, the absence of a rigid magnetic yoke diminishes the structural stiffness of the assembly, requiring additional mechanical reinforcements to ensure dimensional stability under dynamic loading.

From a magnetic perspective, the lack of a well-defined return path increases the complexity of flux confinement and the potential for leakage if rotor pole shapes and material properties are not carefully optimized.

Recent advances in materials science, electromagnetic modeling, and precision additive manufacturing are helping to overcome these limitations. As a result, yokeless axial flux motors are emerging as a compelling alternative to traditional radial flux machines, combining enhanced torque density, reduced weight, and high thermal efficiency with unmatched geometric flexibility.

2 Structure

2.1 Segmented armature: stator teeth and yoke-less design

The stator of the yokeless axial flux motor is composed of a segmented armature structure, a key innovation that eliminates the traditional continuous yoke commonly found in radial flux machines. Each segment consists of an individual stator tooth made of ferromagnetic material, typically a soft magnetic composite (SMC), and is mechanically and magnetically independent from adjacent teeth. This modular architecture offers several advantages.

Geometrically, the teeth are arranged radially and extend axially between the opposing rotor discs, defining the active air gaps where torque is generated. The absence of a surrounding ferromagnetic yoke simplifies the magnetic flux path, which now closes directly between the two facing rotors. This shortens the magnetic circuit and reduces the overall magnetic reluctance. Additionally, the removal of the back iron yoke significantly decreases iron losses, particularly hysteresis and eddy current losses, as the flux path avoids large ferromagnetic return paths. In high-performance applications, where thermal management is critical, each tooth can be thermally optimized individually, enabling superior cooling strategies compared to conventional integrated stators.

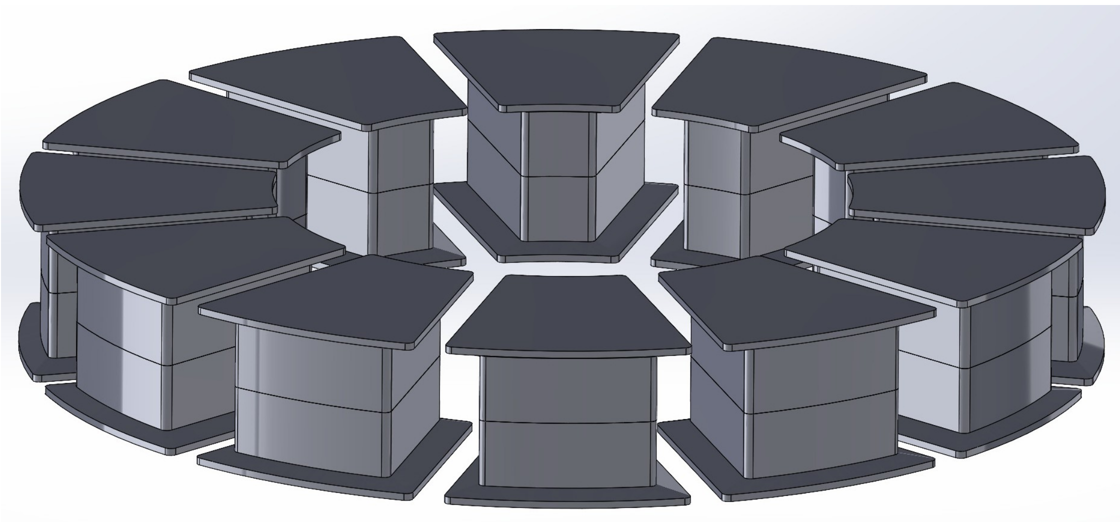

Figure 1.2: Segmented stator teeth in a yokeless axial flux motor

2.2 Rotors and permanent magnets

The rotor system of a double rotor yokeless axial flux motor consists of two co-axial rotating discs mounted on either side of the stator. Each rotor carries a series of permanent magnets positioned on a circular path at equal angular intervals. These magnets are magnetized axially, meaning perpendicular to the plane of the rotor. As a result, one rotor presents north-facing poles toward the stator, while the opposing rotor presents south-facing poles, thus establishing a closed-loop axial magnetic flux path.

The configuration is innovative not only in its geometry but also in its functional performance. By placing the magnets on the interior surfaces of both rotors, the motor generates two active air gaps, increasing the effective area where electromagnetic torque is produced. This contributes directly to higher torque density and improved volumetric efficiency.

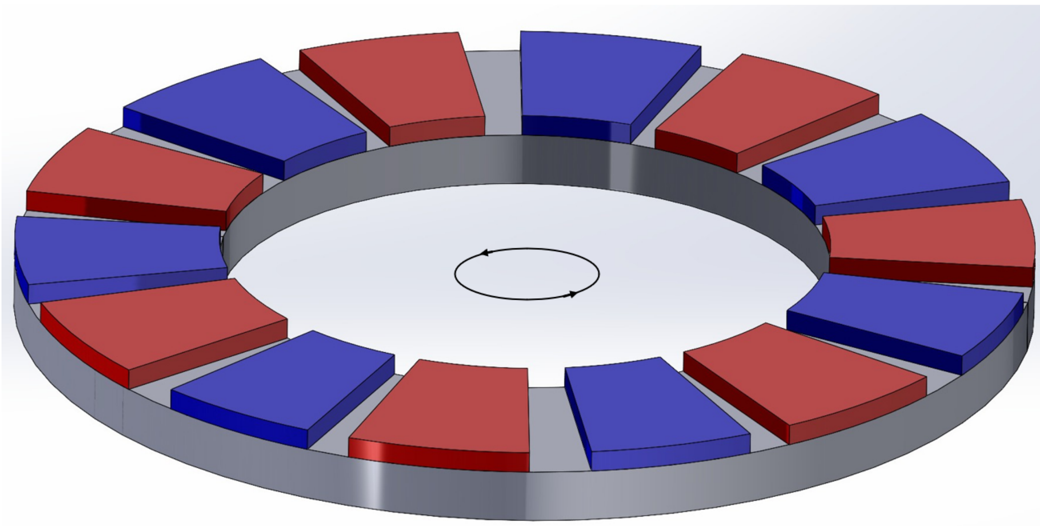

Figure 1.3: Rotors configuration with axially magnetized permanent magnets

A technical consideration arises due to the intense magnetic attraction between the opposing rotors. This attractive force can cause deflection of the rotor discs, particularly in the thin back iron sections supporting the magnets. While minor deformation is expected and tolerable, excessive deflection may lead to a critical reduction in the air gap, risking mechanical interference with the stator. To address this, rotor stiffness must be carefully engineered through material selection and structural reinforcement, ensuring dimensional stability under electromagnetic loading.

2.3 Stator windings

In the yokeless axial flux motor, the windings are embedded directly within each individual stator segment, thereby eliminating the need for coil end turns. Each stator tooth carries a concentrated winding, typically composed of high-conductivity copper. The coils are arranged such that the current flows orthogonally to the axial magnetic field, maximizing the Lorentz force and, consequently, the torque produced.

This configuration significantly enhances copper utilization, as all of the winding volume actively contributes to torque production, unlike in radial machines where substantial portions of the winding reside outside the magnetic gap as non-torque-contributing end windings. The absence of coil ends reduces both Joule losses and parasitic inductance, improving efficiency and dynamic response.

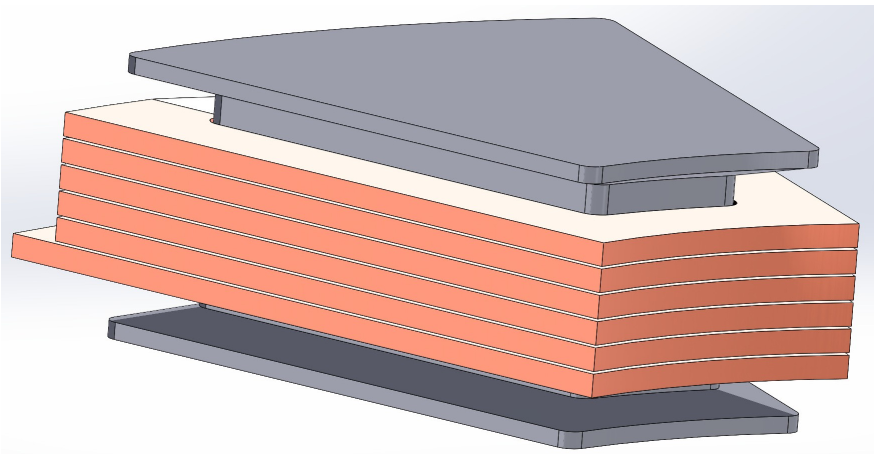

Figure 1.4: Concentrated winding around stator tooth

3 Sources and nature of losses

3.1 Ohmic losses

In electric machines, ohmic losses represent the most significant forms of energy dissipation, especially during steady-state operation under load. These losses arise from the intrinsic resistance of the conductors through which electric current flows, and are a direct consequence of Joule's law, according to which the passage of electric current through a resistive medium causes the conversion of part of the electrical energy into thermal energy. This phenomenon is described by the fundamental relation $P = I^2 R$ where P is the power dissipated as heat, I is the current, and R is the electrical resistance of the conductor. Within an electric motor, Joule losses primarily occur in the windings of the stator, where large currents are required to generate the necessary magnetic fields for torque production. The magnitude of Joule losses depends on several interrelated factors, starting from the choice of conductive material. Copper is commonly used due to its low electrical resistivity, but even in its high-purity form, resistance cannot be entirely eliminated, especially over the long and densely packed windings typical of electric machines. Another critical variable is the geometry and configuration of the windings themselves. Longer winding paths, narrow cross-sections, and compact arrangements all contribute to increased electrical resistance. This becomes particularly problematic at elevated operating temperatures. As the motor heats up, the resistivity of copper increases linearly with temperature, governed by the temperature coefficient of resistance. This results in a positive feedback effect: higher current leads to higher temperatures, which in turn raise the resistance and cause further heating, reducing both the efficiency and reliability of the machine.

While the stator windings represent the primary locus of Joule losses since they directly carry the output current from the inverter the phenomenon is not limited to these conductors alone. Other conductive components within the motor, such as the stator teeth, rotor cores, and even the permanent magnets in high-performance machines, can also be sites of resistive energy dissipation.

This occurs not because of conduction currents originating from the power supply, but due to the induction of circulating currents, known as *eddy currents*, within these components. According to Faraday's law of electromagnetic induction, any conductive material exposed to a time-varying magnetic field will experience the formation of closed-loop currents within its volume.

$$\mathcal{E} = -\frac{d\Phi_B}{dt} \tag{1.1}$$

where:

- $\mathcal{E}$ is the electromotive force $[V]$
- Φ_B is the magnetic flux $[Vs]$
- $\frac{d\Phi_B}{dt}$ is the time derivative of the magnetic flux
- The negative sign reflects Lenz's Law, indicating that the induced EMF opposes the change in flux

The magnetic flux Φ_B through a surface S is defined as:

$$\Phi_B = \int_S \vec{B} \cdot d\vec{A} \tag{1.2}$$

where:

- $\vec{B}$ is the magnetic field vector $[T]$
- $d\vec{A}$ is a differential element of area on the surface S, oriented perpendicularly

In other words, magnetic flux represents the total magnetic field passing through a given surface. When this flux varies over time, it induces an electromotive force in a surrounding conductive loop, as described by Faraday's Law. In the case of conductive materials this electromotive force gives rise to circulating currents within the material itself. These currents flow in closed loops perpendicular to the changing magnetic field and dissipate energy as heat due to the material's electrical resistance thereby contributing to the overall Joule losses of the machine. The geometry, material properties, and frequency of magnetic field variation all influence the extent of these parasitic effects.

For instance, in conductive components eddy currents can become substantial, especially in regions with high flux density variation such as the stator teeth adjacent to the air gap or the surface of rotor magnets. Although these losses are often classified separately as *core losses* due to their association with the ferromagnetic structure, from a physical standpoint they are still resistive losses, governed by Joule's law, and arise from internal currents induced by magnetic rather than electrical excitation. These aspects underscore the complexity of thermal and loss modeling in electric machines, where not only the conduction paths but also the electromagnetic environment must be carefully considered to ensure accurate prediction and minimization of inefficiencies.

3.2 AC losses

Although the underlying physical mechanism of AC losses is identical to that of conventional ohmic losses their origin is specifically related to the effects of alternating current at high frequencies and the associated time-varying magnetic fields. AC losses primarily arise from two electromagnetic phenomena: the *skin effect* and the *proximity effect*. Both effects lead to a non-uniform distribution of current density within conductors, which in turn increases the effective resistance compared to the DC case and thereby enhances the Joule heating within the machine components [1].

The *skin effect* refers to the tendency of alternating current to concentrate near the surface of a conductor rather than being uniformly distributed across its entire cross-section. In direct current conditions, the current density is homogeneous throughout the conductor's cross-section. However, under AC excitation, the situation changes significantly due to electromagnetic induction effects.

As the current varies over time, it generates a time-dependent magnetic field surrounding the conductor. According to Faraday's Law of electromagnetic induction and Lenz's Law, this varying magnetic field induces circulating eddy currents within the conductor itself. These induced currents oppose the changes in the original magnetic field, thereby opposing the flow of current, particularly in the central regions of the conductor.

Consequently, the net current density is no longer uniform: it becomes maximum near the surface and progressively decreases towards the interior. This redistribution effectively reduces the cross-sectional area available for current conduction, which in turn increases the conductor's apparent resistance. The higher the frequency of the alternating current, the more pronounced this effect becomes.

The depth to which the current penetrates into the conductor is characterized by the so-called *skin depth* (δ) defined as:

$$\delta = \sqrt{\frac{2\rho}{\mu\omega}} \tag{1.3}$$

where:

- δ is the skin depth $[m]$
- ρ is the electrical resistivity of the conductor material $[\Omega \cdot m]$
- μ is the magnetic permeability of the material $[H/m]$
- $\omega = 2\pi f$ is the angular frequency of the alternating current $[rad/s]$

Physically, the skin depth represents the distance from the conductor surface at which the current density falls to approximately 37% of its maximum surface value. As frequency increases, δ decreases, leading to a more pronounced concentration of current near the surface.

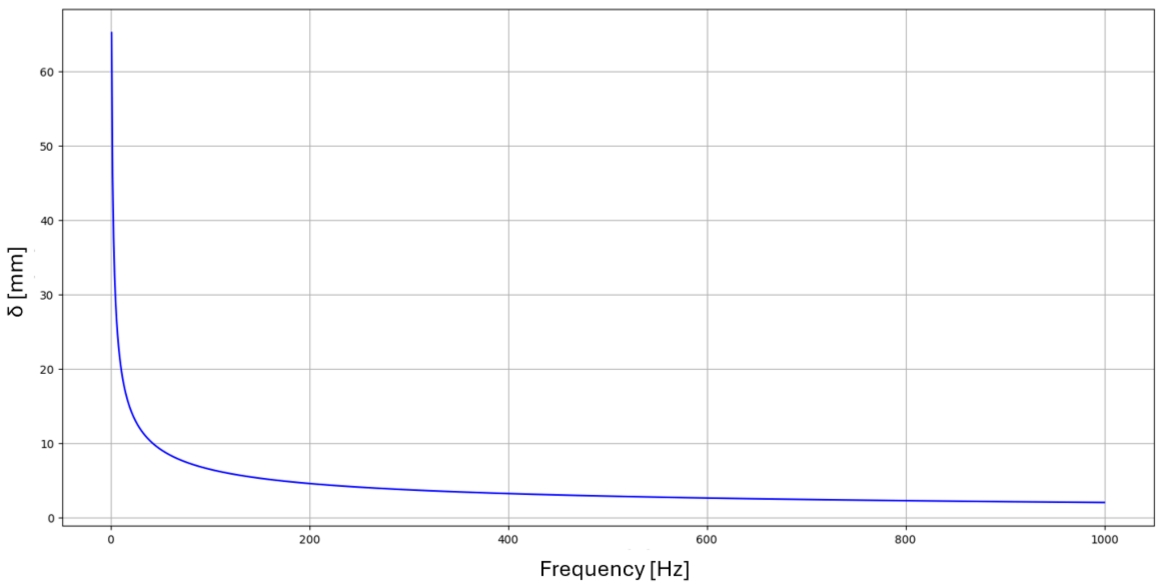

Figure 1.5: Copper skin depth VS frequency at 20 $[°C]$

In high-frequency applications this effect significantly increases conductor resistance and consequently, the associated power losses.

In addition to the skin effect, the *proximity effect* further alters the current distribution within conductors that are situated in close proximity to each other. This phenomenon arises from the mutual magnetic fields generated by neighboring conductors carrying AC currents. Depending on the relative orientation of these currents, the induced magnetic fields can cause the current in a conductor to crowd towards one side of its cross-section, further increasing its effective resistance.

In the context of electric machines, the proximity effect is particularly relevant in stator windings and concentrated winding layouts, where multiple conductors are placed in close quarters. The alternating magnetic fields produced by adjacent conductors lead to asymmetric current density distributions, resulting in localized hotspots and elevated power losses. The severity of the proximity effect increases with frequency, conductor spacing, and the geometrical arrangement of the windings.

It is important to emphasize that both skin and proximity effects ultimately result in energy dissipation through the Joule heating mechanism. However, unlike conventional ohmic losses caused by conduction currents from the power source, these phenomena are driven by *induced currents* arising from electromagnetic interactions.

3.3 Magnetic losses

Magnetic losses represent a significant source of energy dissipation in electric machines operating under alternating magnetic fields. In contrast to ohmic losses, which originate from conduction currents in windings, magnetic losses are caused by the time-varying interaction between magnetic materials and electromagnetic fields. These losses are intrinsically related to the physical and electromagnetic properties of ferromagnetic materials and place important constraints on machine efficiency, thermal behavior, and power density particularly in high-speed or high-frequency applications.

Magnetic losses are primarily associated with *hysteresis*, a phenomenon that occurs during the cyclic magnetization and demagnetization of ferromagnetic cores. At the microscopic scale, hysteresis losses are attributed to the irreversible motion of magnetic domain walls, which face resistance due to crystalline imperfections and internal friction. Each reversal of the magnetic field requires energy to overcome these localized impediments, and this energy is dissipated as heat.

This magnetization behavior is illustrated by the *B-H curve*, which plots the magnetic flux density B $[T]$ as a function of magnetic field strength H $[A/m]$.

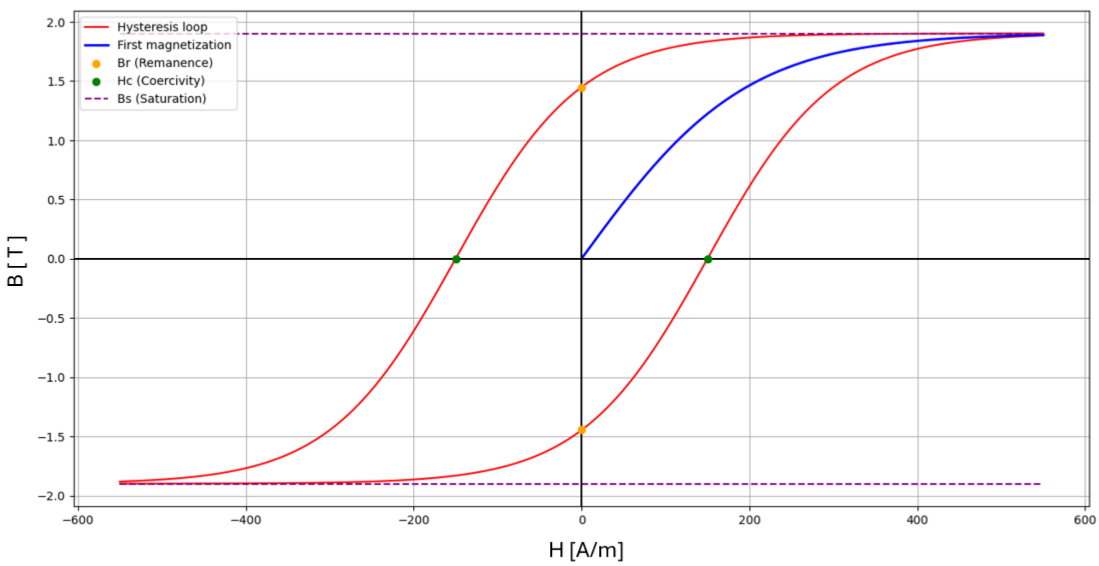

Figure 1.6: B-H curve of a ferromagnetic material

During the initial magnetization process, the material follows a path known as the *first magnetization curve*, represented by the blue trajectory. This curve characterizes the response of a previously unmagnetized material to an increasing magnetic field. Once the material has been magnetized and is subjected to cyclic excitation, the B–H relationship no longer retraces the same path but instead forms a closed loop known as the *hysteresis loop*. This loop illustrates the phase lag between the applied magnetic field strength H and the resulting magnetic flux density B. The area enclosed by this loop quantitatively represents the energy dissipated per unit volume during each cycle and is directly proportional to the hysteresis losses. These losses increase with both the frequency of the magnetic excitation and the material-specific characteristics of the B-H curve.

The geometry of the hysteresis loop is governed by key magnetic parameters of the material: *Coercivity* denotes the magnetic field strength required to reduce the flux density to zero after the material has been saturated. Materials with high coercivity exhibit broader hysteresis loops and consequently higher energy losses. *Saturation magnetization* represents the maximum flux density a material can support; a higher saturation value enables the core to operate efficiently at strong field levels without significant nonlinear distortion. *Remanence* describes the residual magnetization that persists after the external field is removed. Higher remanence leads to increased hysteresis area and associated losses. Therefore, materials used in motor cores are typically optimized to exhibit low coercivity, low remanence, and sufficiently high saturation magnetization, all of which help minimize magnetic losses and enhance thermal stability.

In yokeless axial flux machines, magnetic losses are primarily concentrated in the stator teeth, where variations in flux are most intense, and to a lesser extent in the rotor back iron supporting the permanent magnets. The absence of a yoke results in a stator composed of modular magnetic segments that efficiently guide axial magnetic flux between the two opposing rotors. While this design minimizes magnetic path length and reduces reluctance, it also leads to highly localized magnetic field variations, which complicate the task of loss control.

To estimate magnetic losses, several empirical models have been proposed. One of the most widely used is the *classical Steinmetz equation (CSE)* [2], introduced in the late 19th century. It offers a practical method for estimating power loss in ferromagnetic materials under sinusoidal excitation:

$$P = k \cdot f^{\alpha} \cdot B_{\text{max}}^{\beta} \tag{1.4}$$

where P is the specific power loss [W/m^3], f is the frequency [Hz], B_{max} is the peak flux density [T], and k, α, and β are empirical Steinmetz coefficients that depend on the material.

These coefficients summarize how the material responds to periodic magnetization. The exponent α captures the frequency dependence of the losses, while β reflects the nonlinear relationship between loss and flux density. The constant k scales the magnitude of the loss based on intrinsic material properties.

While the classical Steinmetz equation is effective for sinusoidal waveforms and moderate frequencies, it falls short when applied to nonsinusoidal or high-frequency excitations. To overcome this, more advanced models have been developed. One of the most notable is the *Bertotti loss model*[3], which offers a more physically rigorous approach by decomposing the total power loss into three additive components:

$$P_{\text{total}} = P_{\text{hyst}} + P_{\text{eddy}} + P_{\text{excess}} \tag{1.5}$$

where P_{hyst} is the hysteresis loss, P_{eddy} is the classical eddy current loss and P_{excess} accounts for dynamic losses associated with rapid domain wall displacements and microstructural interactions, which become significant at high frequencies.

An additional refinement, particularly relevant for power electronics and inverter-driven machines, is the *Generalized Steinmetz Equation (GSE)*. This formulation extends the classical model to arbitrary time-varying flux waveforms by integrating the instantaneous rate of change of the flux density:

$$P_v = \frac{1}{T}\int_0^T k \left|\frac{dB(t)}{dt}\right|^{\alpha} B(t)^{\beta-\alpha}\, dt \tag{1.6}$$

where $B(t)$ is the time-dependent magnetic flux density, T is the excitation period, and k, α, and β are again material-dependent parameters.

Despite its simplifications, the Steinmetz model in its classical forms remains a cornerstone in magnetic loss analysis, providing engineers with a practical and scalable approach for estimating energy dissipation in magnetic cores.

In conclusion, magnetic losses represent a critical limitation in the design of high-efficiency electric machines. Their underlying physical mechanisms are well understood, yet minimizing them remains an active area of research due to the complex interplay between electromagnetic excitation, material properties, and thermal constraints. For yokeless axial flux machines, where magnetic flux distribution is highly concentrated and nonuniform, careful modeling and material optimization are essential for achieving high performance and system reliability.

2. Additive manufacturing

1 Introduction

Additive Manufacturing (AM) is a transformative manufacturing paradigm that enables the creation of three-dimensional parts directly from digital models through a layer-by-layer deposition approach. This methodology contrasts with traditional subtractive and formative processes by joining material only where needed, reducing waste and often eliminating the need for tooling. Originally developed under the term Rapid Prototyping (RP), AM has progressively evolved beyond prototyping into a viable strategy for final part production. This shift has found widespread application in aerospace, biomedical, energy, and, to a lesser extent, automotive sectors, largely due to the capacity of AM technologies to deliver geometrically complex and high-performance components [4].

A significant advantage of AM lies in its design freedom: complex geometries, internal lattice structures, and internal cooling channels, previously impossible or prohibitively expensive to fabricate, can now be realized without the constraints of traditional manufacturing. Moreover, AM permits the consolidation of multiple parts into a single component, reducing assembly requirements and enhancing structural integrity. These features are particularly valuable in lightweighting strategies and customized product development, contributing to increased functional performance and reduced lifecycle costs.

In addition to design flexibility, AM supports a broad spectrum of materials, including polymers, ceramics, metals, and bio-materials. This versatility simplifies the manufacturing of complex parts directly from 3D CAD data, removing the need for molds or complex tooling. The layer-wise nature of the process allows for precise control of geometry, which is especially important in applications where accuracy and shape complexity are critical.

The AM process begins with the creation of a solid CAD model, which is then converted into a stereolithography (STL) file. This format tessellates the geometry into triangular facets, forming the basis for subsequent layer generation. All AM systems use a layer-based approach, in which a 3D object is constructed by successively adding thin horizontal slices. Although all AM technologies follow this principle, they differ in terms of the materials used, the method of layer formation (e.g., melting, deposition, extrusion), and the bonding mechanisms, each of which affects dimensional accuracy, material properties, production speed, and post-processing requirements.

The standard ISO/ASTM 52900:2021 [5] identifies seven primary categories of AM processes, each defined by the method of material deposition and energy application.

- **Directed Energy Deposition (DED)**: Material, in powder or wire form, is fed and melted simultaneously by a focused energy source (laser, electron beam, or plasma). Commonly used for large parts, repairs, and hybrid manufacturing.
- **Material Extrusion (MEX)**: Semi-molten thermoplastic or metal filament is extruded through a nozzle and solidifies on cooling. Known for low cost and accessibility, though limited in resolution.
- **Powder Bed Fusion (PBF)**: Thermal energy selectively melts powder to form dense parts. Offers high precision and material properties close to wrought metals, especially for aerospace and medical use.
- **Material Jetting (MJT)**: Droplets of material (e.g., photopolymer or wax) are deposited and cured with UV light. Offers high resolution and multi-material capability, but with limited mechanical strength.
- **Sheet Lamination (SHL)**: Layers of sheet material are bonded together, often after being pre-cut. Fast and low-cost, but less suitable for high-strength applications.
- **Vat Photopolymerization (VPP)**: A light source selectively cures resin in a liquid vat. Delivers excellent detail and surface finish, mainly for prototyping.

Among these, Powder Bed Fusion is particularly noteworthy for its ability to process both polymers and metals with high precision and excellent mechanical properties. In L-PBF a high-brilliance laser selectively melts regions of a thin metal powder layer within a controlled build environment.

The process begins by spreading a uniform powder layer onto a build platform. A laser beam is then directed onto the bed by galvanometric mirrors, selectively scanning cross-sections of the part geometry. The laser fully melts the metal powder to form a molten pool, which subsequently solidifies and bonds with previously deposited layers. This process repeats iteratively, layer by layer, to build the complete part. The build chamber is typically filled with inert gases such as nitrogen or argon to prevent oxidation and manage heat dissipation. Process gases also play a crucial role in stabilizing the melt pool by removing spatter and metal vapors, and in minimizing powder displacement caused by vapor recoil pressure generated during laser-material interaction [6].

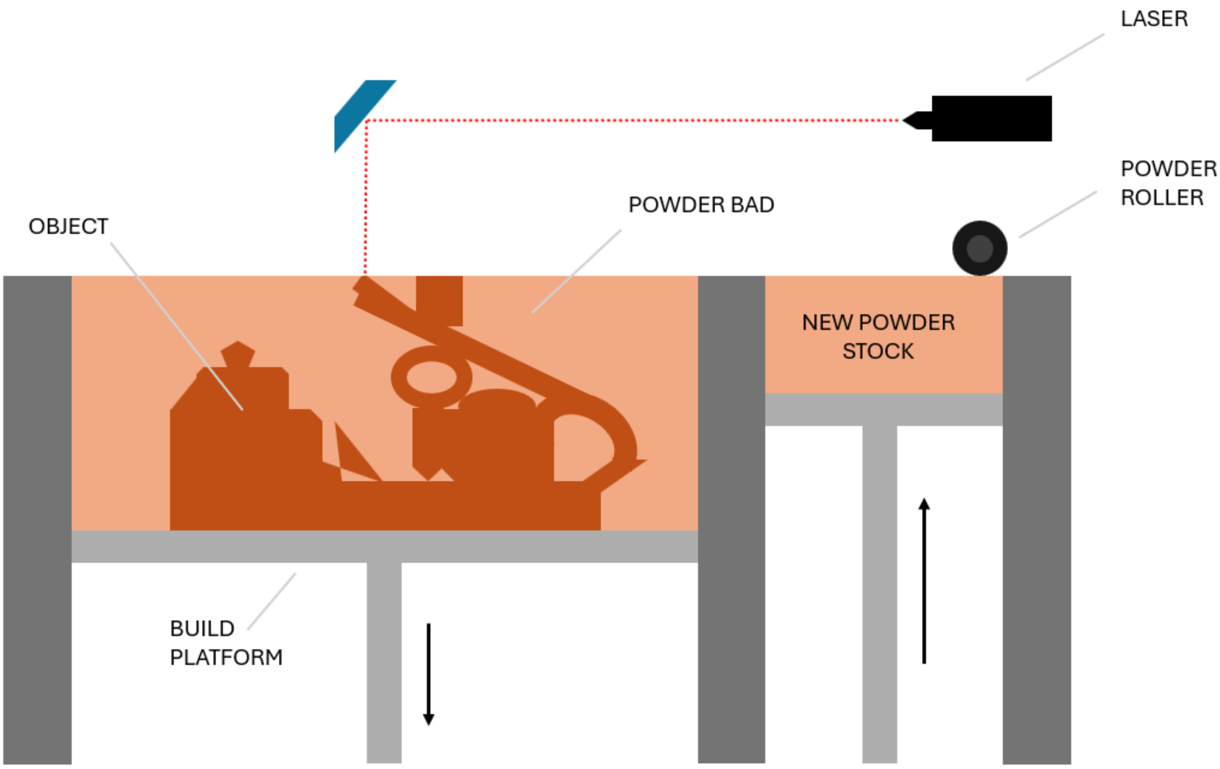

Figure 2.1: Laser powder bed fusion

Despite its advantages, L-PBF presents several technical challenges. The localized and intense energy input results in steep thermal gradients, which can induce significant residual stresses and deformation. These must be mitigated through appropriate support structures and sometimes post-processing heat treatments. Furthermore, the relatively low thermal conductivity of the powder bed compared to bulk metal necessitates support structures for overhanging features beyond a critical angle, commonly 45°, to ensure adequate heat dissipation during fabrication. Cracking may occur due to differential thermal contraction between successive layers, while porosity remains a primary concern [7].

From a cost perspective, L-PBF demonstrates unique characteristics. Unlike traditional manufacturing methods, the cost of a part produced via L-PBF is largely independent of geometric complexity. This makes it highly competitive for producing intricate components. However, the unit cost does not scale significantly with batch size, limiting its economic viability in large-scale serial production. The build volume, part orientation, and packing density are critical factors in determining throughput and cost-efficiency.

In summary, L-PBF represents one of the most advanced and versatile metal additive manufacturing techniques available today. Its capacity to produce fully dense, mechanically robust parts with intricate geometries makes it ideal for high-value, low-volume applications. However, the technology requires meticulous process control and parameter optimization to avoid defects and ensure repeatable quality. As the technology matures, continued advancements in machine architecture, process monitoring, and material development are expected to further expand its industrial adoption. AM's advantages including minimal material waste, rapid prototyping, flexibility in design iteration, and the ability to use a wide range of materials, continue to redefine the boundaries of modern manufacturing.

2 Copper

Copper, with atomic number 29, is a transition metal whose exceptional electrical and thermal properties are fundamentally rooted in its atomic and crystallographic structure. Its electronic configuration, $[Ar] \cdot 3d^{10} \cdot 4s^1$, features a completely filled 3d subshell and a single loosely bound 4s electron. This 4s electron plays a central role in electrical conduction, as it is readily delocalized across the metallic lattice, forming the basis for copper's outstanding conductivity. Structurally, copper crystallizes in a face-centered cubic (FCC) lattice, which is characterized by high symmetry and atomic packing efficiency.

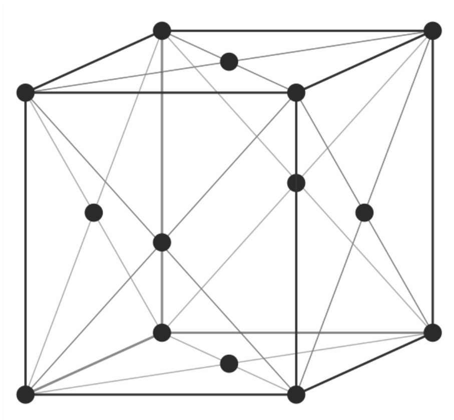

Figure 2.2: Face-centered cubic lattice

Each copper atom is surrounded by twelve nearest neighbors, facilitating efficient electron movement and reducing resistive scattering. The FCC arrangement not only enhances conductivity but also contributes to copper's high ductility and malleability, allowing it to be easily drawn into thin wires, an essential attribute for its widespread use in electrical wiring. From a materials science perspective, the FCC lattice offers minimal resistance to dislocation motion, making copper relatively soft and mechanically compliant. On a macroscopic scale, copper is among the best conductors of electricity, second only to silver. This performance is attributed to the broad conduction band formed by overlapping atomic orbitals in the FCC structure, which permits free movement of electrons under an applied electric field.

At 20 $[^\circ C]$ copper exhibits an extremely low resistivity of approximately 1.68×10^{-8} $[\Omega \cdot m]$. However, as temperature increases, thermal lattice vibrations intensify, causing more frequent scattering of conduction electrons and consequently leading to an increase in resistivity. This behavior is quantified by a positive temperature coefficient of resistance. The temperature dependence of copper's electrical conductivity $\sigma(T)$ can be expressed as:

$$\sigma(T) = \frac{1}{\rho_0[1 + \alpha(T - T_0)]} \text{ [S/m]} \tag{2.1}$$

where the reference values are $\alpha = 0.0039$ $[^\circ C^{-1}]$, $\rho_0 = 1.68 \times 10^{-8}$ $[\Omega \cdot m]$, and $T_0 = 20$ $[^\circ C]$. Substituting these into the equation yields:

$$\sigma(T) = \frac{1}{1.68 \times 10^{-8}[1 + 0.00393(T - 20)]} \text{ [S/m]} \tag{2.2}$$

This relationship illustrates the inverse correlation between temperature and electrical conductivity.

Despite this temperature sensitivity, copper maintains a long mean free path for conduction electrons, which allows it to preserve high conductivity over a broad range of operating conditions.

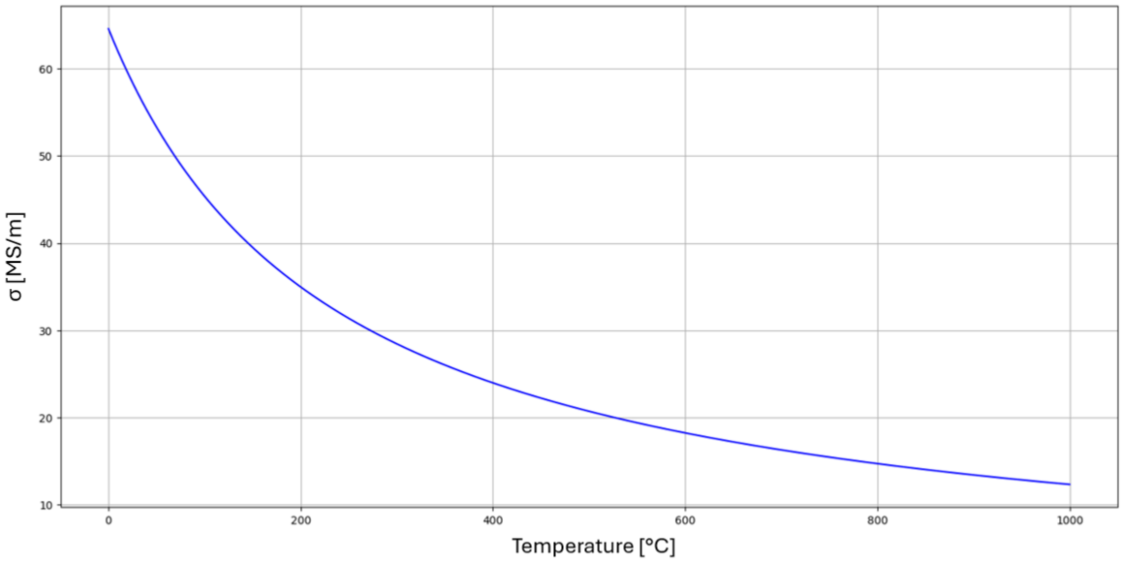

Figure 2.3: Copper electrical conductivity VS temperature

Moreover, copper exhibits excellent thermal conductivity, with a thermal conductivity coefficient of approximately 400 $[\frac{W}{m \cdot K}]$ at 20 $[°C]$. This outstanding thermal transport capability is primarily attributed to the same free electrons responsible for its electrical conductivity. The relationship between electrical and thermal conduction in metals is described by the *Wiedemann–Franz-Lorenz law* [8], which states that the ratio between the thermal conductivity κ and the electrical conductivity σ is proportional to the absolute temperature T:

$$\frac{\kappa}{\sigma} = L \cdot T \tag{2.3}$$

where L is the Lorenz number, approximately equal to 2.45×10^{-8} $[\frac{W \cdot \Omega}{K^2}]$. This law reflects the fact that, in metals like copper, both charge and heat are transported predominantly by delocalized electrons. As a result, materials with high electrical conductivity also exhibit high thermal conductivity, which is a critical advantage in applications requiring efficient heat dissipation, such as electric windings, busbars, and thermal interfaces in power electronics.

In addition to its conductive and thermal properties, copper exhibits a unique electromagnetic behavior due to its atomic structure. The absence of unpaired electrons in its ground state results in the lack of permanent magnetic moments, rendering copper a diamagnetic material. When exposed to an external magnetic field, copper develops a weak, opposing magnetic field induced by the orbital motion of electrons in accordance with Lenz's Law. These induced microscopic circulating currents generate a field that counteracts the applied field, giving rise to a weak but measurable diamagnetic response. The magnetic susceptibility (χ) of copper is small and negative, and its relative magnetic permeability is slightly less than unity, with $\mu_r = 1 + \chi \approx 0.999994$. This indicates that the magnetic field inside copper is marginally attenuated compared to a vacuum. The lack of unpaired electrons precludes any form of magnetic ordering, such as paramagnetism or ferromagnetism, even at very low temperatures. The electromagnetic neutrality of copper ensures that its conduction electrons experience minimal spin-related scattering, further enhancing its electrical performance. In summary, copper's exceptional conductivity and negligible magnetic interference arise from a rare combination of atomic-scale electronic stability and a crystallographic structure that supports efficient charge transport and minimal resistance to external perturbations.

3 Laser powder bed fusion of pure copper

Whil L-PBF is widely recognized for its ability to fabricate high-performance metallic components, the additive manufacturing of pure copper presents unique challenges due to its intrinsic physical properties. Copper is a highly conductive material not only electrically and thermally, but also optically in the infrared spectrum. This latter characteristic results in a very high reflectivity to standard near-infrared laser sources, such as the commonly used ytterbium fiber lasers [9]. In practical terms, this means that a significant portion of the incident laser energy is reflected rather than absorbed, reducing process efficiency and leading to unstable melting behavior. Moreover, copper's high thermal conductivity rapidly dissipates heat away from the melt pool, which limits the local temperature rise and complicates the achievement of full melting and bonding between layers. These factors together necessitate the use of higher laser powers, typically above 1 $[kW]$, along with careful parameter optimization to stabilize the melt pool and achieve dense, defect-free builds.

Despite these challenges, the additive manufacturing of pure copper via L-PBF offers substantial opportunities, particularly in applications where the material's superior electrical and thermal performance can be fully leveraged. In the energy sector, for example, copper's low electrical resistivity is invaluable for the production of high-efficiency conductors and connectors. Additive manufacturing enables the fabrication of complex geometries, such as hollow or cooled conductors, that are otherwise impossible or economically unfeasible with conventional subtractive methods. Similarly, in the field of power electronics and electromechanical systems, L-PBF allows for the design and integration of intricate copper windings, coils, and inductive components directly into structural parts or housings, minimizing interconnect losses and improving thermal management.

Electric motors represent another high-impact application area. The possibility of printing custom-shaped copper windings with optimized cooling channels can lead to significant improvements in power density, thermal dissipation, and weight reduction.

Traditional winding techniques often impose geometric constraints and require complex assemblies; by contrast, L-PBF enables the integration of copper coils directly into stator cores, reducing assembly steps and contact resistances. In RF and microwave applications, where high-frequency current transport demands superior surface conductivity, additively manufactured pure copper can be used to fabricate high-precision waveguides, antenna feeds, and resonators with internal features designed for optimal electromagnetic performance.

The successful use of L-PBF for copper also depends on the quality of the powder feedstock. High-purity, gas-atomized copper powders with spherical morphology and narrow particle size distributions are essential to ensure good flowability and consistent layer deposition. Moreover, process control strategies, including real-time melt pool monitoring, adaptive scanning strategies, and optimized scanning paths, are critical for mitigating common defects such as porosity, lack of fusion, and surface roughness. In recent years, advances in laser source technology including the use of green lasers which are more readily absorbed by copper, have further improved the viability of additive manufacturing for this material.

In conclusion, while pure copper poses considerable challenges to laser-based additive manufacturing due to its high reflectivity and thermal conductivity, the technological and functional benefits of producing copper components via L-PBF are substantial. The ability to fabricate complex, high-performance electrical and thermal components unlocks new design paradigms in energy, automotive, aerospace, and electronics industries. As laser and material technologies continue to advance, L-PBF is poised to become a strategic enabler for next-generation copper-based systems.

3. Design of an axial flux motor with hollow windings

1 Introduction

The experimental phase of this thesis focuses on the investigation of stator windings with integrated internal cooling channels, manufactured via pure copper additive manufacturing. Specifically, the study targets a yokeless axial flux motor architecture incorporating twelve stator windings and fourteen rotor poles. This 12/14 configuration, commonly adopted in electric machine design, is known for offering a good compromise between electromagnetic performance and mechanical symmetry. It enables low torque ripple and favorable winding distribution, making it a suitable candidate for investigating the implementation of hollow-coil technologies.

To evaluate the feasibility and performance implications of this novel winding approach, a multiphysics simulation strategy was employed using COMSOL Multiphysics. This finite element analysis (FEA) software environment allows for coupled simulations that incorporate electromagnetic, thermal, and fluid dynamic effects, all of which are essential for accurately modeling the operation of internally cooled coils.

Finite element analysis is a numerical technique used to approximate solutions to complex physical problems by discretizing the geometry into small elements (a mesh). Each element follows the governing equations of the system, such as Maxwell's equations for electromagnetics or Navier-Stokes equations for fluid dynamics, and the collective solution of all elements provides an approximate yet highly accurate representation of the physical behavior of the entire system. This method is particularly useful in cases involving spatially varying fields and complex geometries, as is the case in this study.

Two distinct simulation workflows were developed to analyze the performance of the hollow copper windings.

The first simulation was a localized multiphysics model involving a single hollow conductor and the internal flow of cooling water. A sinusoidal current was applied to the ends of the conductor while a constant volumetric water flow was imposed through its internal channels. The simulation was run until steady-state thermal conditions were achieved, and the temperature distribution in both the copper and the coolant was evaluated. Importantly, this simulation allowed the copper's electrical conductivity to be modeled as a function of temperature, thereby capturing the coupled electrothermal behavior of the system. As the electric current generates heat via Joule losses, the internal water flow works to dissipate this heat, enabling higher current densities than would be possible with passive cooling alone.

A parametric study was conducted by varying the inlet flow velocity and applied current amplitude to identify the optimal operating point that maximizes current density while maintaining the copper temperature and fluid pressure below predefined thresholds. Based on the results of this simulation, the internal geometry of the coil and the coolant channels was progressively refined to improve thermal exchange efficiency and reduce hydraulic impedance. The goal was to design a coil structure that supports high current loading while ensuring effective and reliable internal heat extraction with minimal pumping power.

The second simulation focused on the full electromagnetic and electromechanical behavior of the motor under operational conditions. To reduce computational load while preserving generality, spatial symmetries inherent to the 12-slot, 14-pole, double-rotor configuration were exploited. Specifically, the model simulated only one quarter of the machine geometry: six stator coils and seven permanent magnets on a single rotor, leveraging mirror symmetry across axial and radial planes.

Furthermore, given the periodic nature of the current excitation in three-phase synchronous machines, it is sufficient to simulate a single electrical period. In this case, the electrical frequency was set to $f_{el} = 280\,[Hz]$, corresponding to a time interval of one period $T_{el} = 1/f_{el} \approx 3.57\,[ms]$.

The copper temperature and corresponding conductivity values obtained from the multiphysics thermal model were used as inputs in this simulation, ensuring a consistent and realistic representation of material properties.

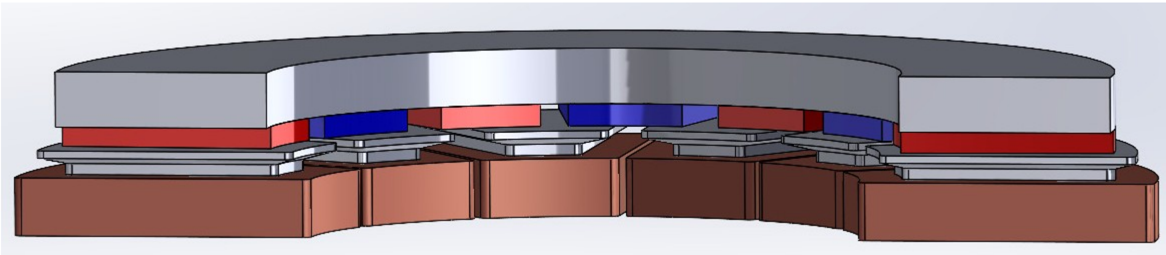

Figure 3.1: Actual simulated volume (quarter of motor)

This electromagnetic simulation yielded key performance indicators of the motor, including output torque, torque ripple, mechanical power, electrical input power, efficiency, and detailed breakdowns of power losses in each motor component. These results provide a comprehensive characterization of the impact of internally cooled hollow windings on motor performance and support the development of more compact, thermally efficient, and power-dense electric machines.

2 Multiphysics coil simulation

2.1 Coil geometry

The geometry of the hollow coil and its internal cooling channel has been optimized to maximize spatial efficiency within the motor while conforming to the geometry of the stator teeth. Thanks to the precision and design freedom of additive manufacturing, each winding is produced with an internal fluidic channel and a perfectly rectangular cross-section, allowing superior space utilization compared to traditional round wires.

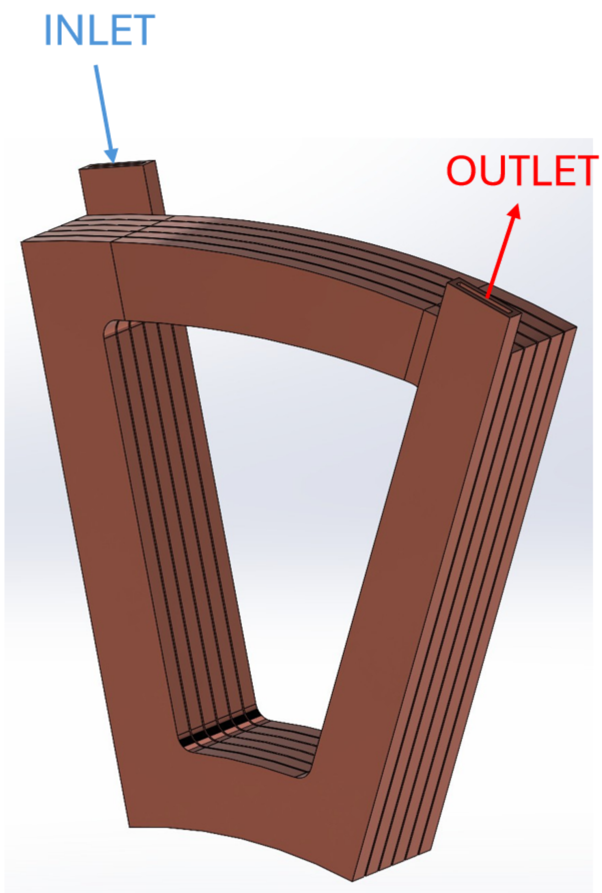

Figure 3.2: Geometry of the hollow winding called *SC1214*

The final winding assembly consists of multiple materials, each selected to perform specific functional requirements. In addition to the additively manufactured hollow copper coil, electrical insulation between adjacent turns is ensured by embedding the windings in an electrically insulating resin, shown in gray in Figure 3.3. This resin not only prevents electrical short-circuits between turns, but also contributes to the mechanical rigidity and structural stability of the coil assembly.

Over time, however, the resin may experience degradation due to mechanical vibrations and thermal cycling during motor operation, potentially leading to the formation of microcracks. To ensure long-term electrical reliability, the entire resin-encapsulated coil is wrapped with a thin layer of Kapton tape, represented in yellow in Figure 3.3. Kapton is a high-performance polyimide film known for its excellent dielectric strength, thermal stability, and resistance to chemical attack. Its inclusion provides an additional layer of insulation, maintaining electrical isolation even in the event of local resin failure. The coil dimensions and materials are summarized in Table 3.1.

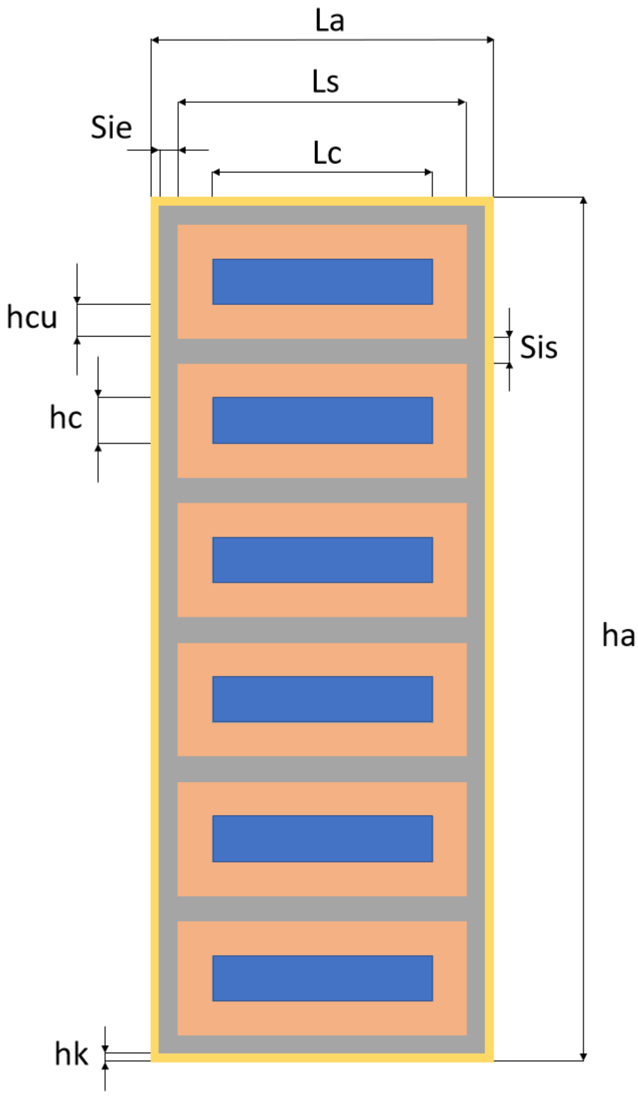

Figure 3.3: *SC1214* section geometry

Once the resin has fully cured and the Kapton tape has been applied around the entire coil assembly, the result is a compact, solid, and mechanically robust block encapsulating the hollow copper winding. This resin-encapsulation process constitutes a significant innovation, as it not only ensures electrical insulation but also imparts structural rigidity to the winding. The solidified resin and Kapton wrapping together transform the flexible coil into a mechanically stable component capable of withstanding the mechanical stresses and thermal cycling typical of electric motor operation.

[ha] Winding height	19 $[mm]$
[La] Winding width	11.52 $[mm]$
[Ls] Turn width	10.66 $[mm]$
Number of turns	6
[hcu] Copper height	0.9 $[mm]$
[Lc] Duct width	8.86 $[mm]$
[hc] Duct height	0.973 $[mm]$
[Sie] Outer insulation height	0.3 $[mm]$
[Sis] Inter-turn insulation height	0.3 $[mm]$
[hk] Kapton height	0.13 $[mm]$
Winding area	218.8 $[mm^2]$
Copper area	125.62 $[mm^2]$
Duct area	51.73 $[mm^2]$
Insulation area	41.45 $[mm^2]$
Fill factor	0.574

Table 3.1: Hollow coil geometry

A key performance parameter is the coil fill factor, defined as the ratio between the cross-sectional area of the copper and the total cross-sectional area of the entire winding. This parameter directly influences the electrical modeling and is used as a primary input in the subsequent simulation phase.

2.2 Energy transport

In the multiphysics simulation developed in COMSOL, three coupled physical domains are simultaneously solved to accurately capture the thermal behavior of the hollow coil during operation. These include electric currents, laminar fluid flow, and heat transfer in solids and fluids.

The first physics models the current distribution within the copper conductor. Once the electrical current inlet terminal and ground are defined, the simulation solves for the electric potential and returns the resulting current density throughout the conductor. This allows the calculation of Joule heating as a function of both current density and local electrical resistivity.

The second physics involves a laminar flow model applied to the internal cooling channel. Given boundary conditions at the inlet and outlet, such as the prescribed velocity of the fluid at the inlet and ambient pressure at the outlet, the model computes the velocity field, streamlines, and pressure distribution along the coolant path.

The third physics interface is dedicated to heat transfer in solids and fluids. It governs the temperature evolution of both the copper winding and the coolant. Heat exchange between the copper and the ambient environment is modeled through two mechanisms: convective heat transfer and thermal radiation. A convective heat flux boundary condition is imposed on the outer copper surfaces with a heat transfer coefficient of 10 $[W/m^2K]$, representing natural convection to air under ambient conditions. In parallel, a surface-to-ambient radiation boundary condition is defined with a surface emissivity of 0.7. The surface emissivity is a material-specific property that quantifies the effectiveness with which a surface emits thermal radiation compared to an ideal blackbody.

As this is a true multiphysics simulation, all physical domains are bidirectionally coupled. The electric current flowing through the copper generates resistive heating, which raises the conductor's temperature. This temperature, in turn, alters the copper's electrical conductivity, since it is modeled as a temperature-dependent property. Simultaneously, heat is transferred from the copper to the flowing coolant through the internal channel walls, and to the surrounding environment via the external surfaces, accounting for both convective and radiative modes of energy transport.

The boundary conditions and material properties used for the simulation are summarized in Table 3.2.

Water inlet temperature	20 $[°C]$
Ambient external temperature	20 $[°C]$
Convective heat transfer coefficient	10 $[W/m^2K]$
Surface emissivity	0.7

Table 3.2: Thermofluidic boundary conditions used in the multiphysics model

2.3 Inlet velocity sweep

To identify the most suitable inlet velocity for the coolant flow, a parametric sweep was conducted in which the inlet water velocity was systematically varied. The simulation was performed using the thermofluidic boundary conditions defined previously in Table 3.2, with the coil subjected to a sinusoidal current excitation defined as:

$$i(t) = \sqrt{2} \cdot I_{\text{RMS}} \cdot \sin(2\pi f_{el} t) \quad \text{with} \quad I_{\text{RMS}} = 414\,[A], \quad f_{el} = 280\,[Hz] \tag{3.1}$$

The electrical frequency f_{el} used in the simulation is not arbitrarily chosen, but instead derived from the mechanical rotation speed of the motor and its pole pair configuration. For synchronous machines, the relationship between electrical frequency f_{el}, mechanical rotational speed n (in RPM), and number of pole pairs P is given by:

$$f_{el} = \frac{P \cdot n}{60} \tag{3.2}$$

In this study, the motor is assumed to operate at a mechanical speed of $n = 2400\,[RPM]$ with a pole configuration of $2P = 14$ (i.e., $P = 7$), resulting in an electrical frequency of:

$$f_{el} = \frac{7 \cdot 2400}{60} = 280\,[Hz]$$

This frequency is then used to define the time-varying sinusoidal current applied to the coil.

The results of the simulation sweep are summarized in the two plots below. Figure 3.4 shows the evolution of the average temperature in both the copper and coolant as a function of inlet velocity, while Figure 3.8 reports the corresponding pressure drop across the fluidic channel.

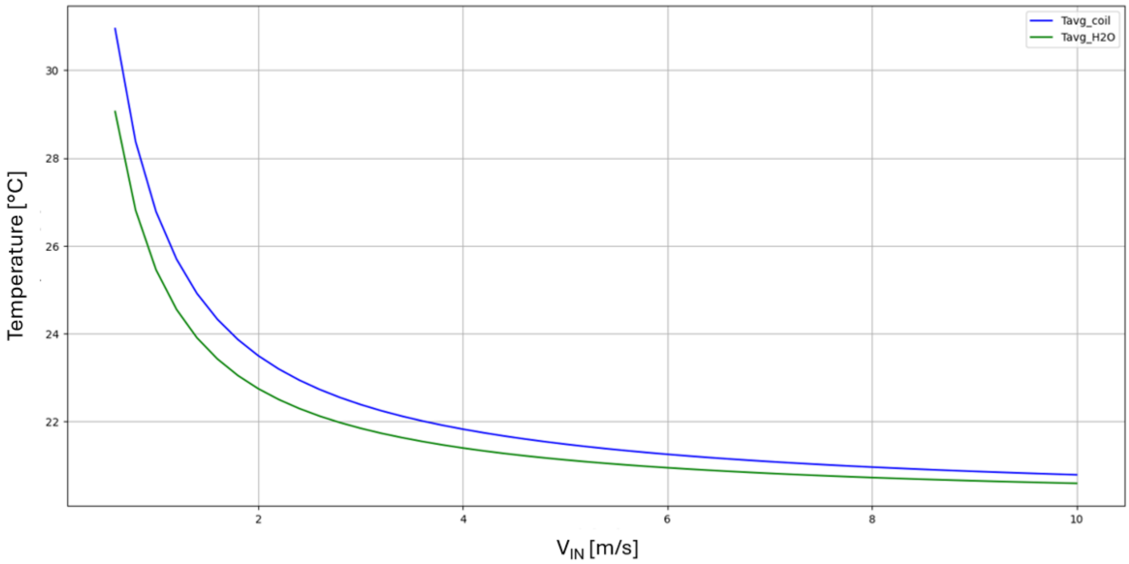

Figure 3.4: Average temperatures VS inlet velocity

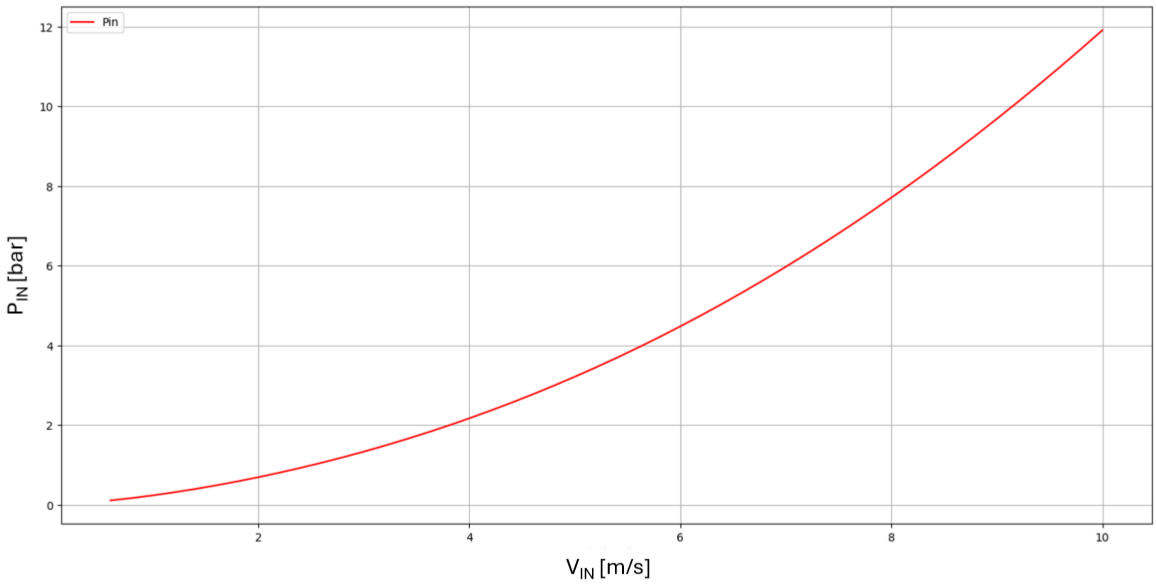

Figure 3.5: Pressure drop VS inlet velocity

Based on the trade-off between thermal performance and hydraulic resistance, an inlet velocity of $4\,[m/s]$ was selected. As evident from Figure 3.4, this flow rate ensures excellent heat exchange between the copper and the coolant, with a temperature difference of only $0.47\,[^{\circ}C]$ between their respective average values. Such a minimal thermal gradient indicates highly efficient heat transfer, which is essential to keeping the winding temperature below critical thresholds. At this velocity, the corresponding pressure drop across the fluidic channel is approximately 2.19 $[bar]$, while the volumetric flow rate reaches 2.07 $[L/min]$. These values are within acceptable limits for integration into a closed-loop cooling system, striking an effective balance between thermal regulation and pumping power consumption.

I_{RMS}	414 $[A]$
Inlet velocity	4 $[m/s]$
Pressure	2.19 $[bar]$
$T_{AVG}\, copper$	21.84 $[°C]$
$T_{AVG}\, H2O$	21.37 $[°C]$
Volumetric flow rate	2.07 $[L/min]$

Table 3.3: Multiphysics simulation results

Figures 3.6, 3.7, and 3.8 present the spatial distributions of temperature, electrical conductivity, and pressure, respectively, as obtained from the multiphysics simulation.

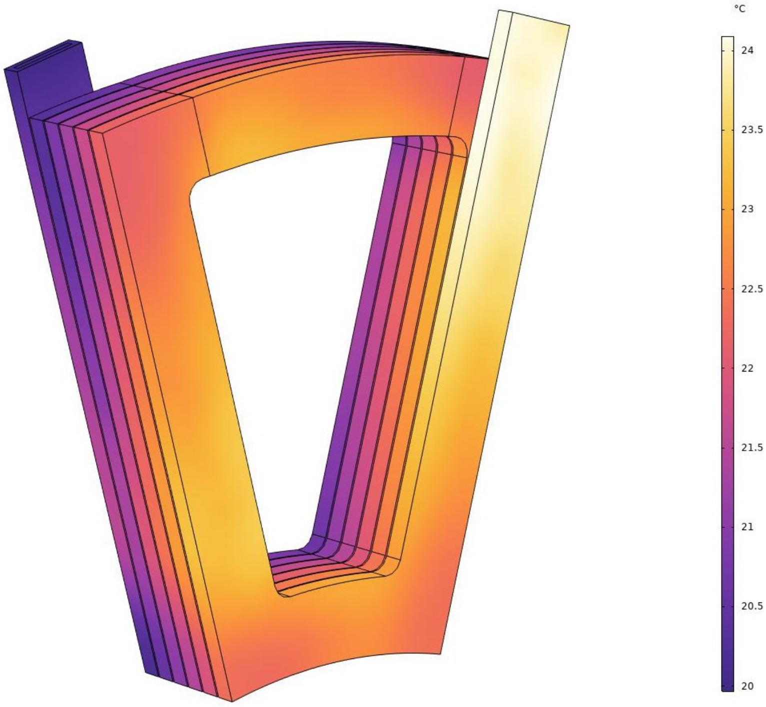

Figure 3.6: Temperature [$^{\circ}C$]

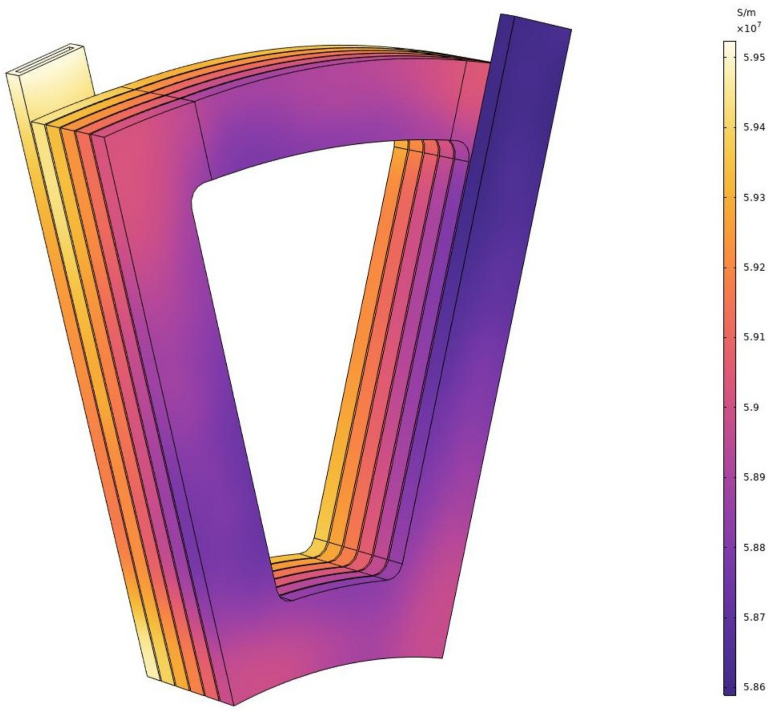

Figure 3.7: Electrical conductivity [S/m]

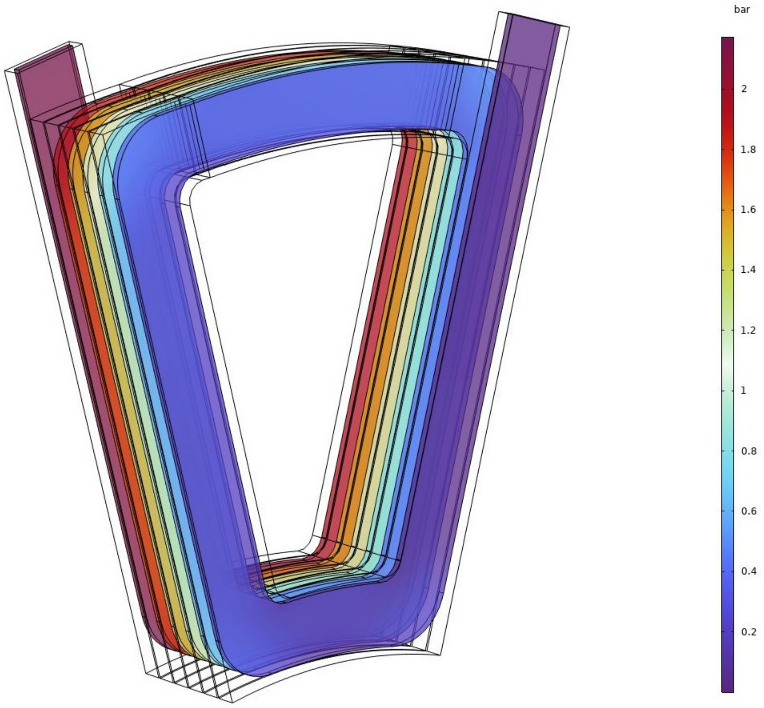

Figure 3.8: Pressure [bar]

A particularly insightful observation arises from the comparison between the temperature and the electrical conductivity maps. According to the temperature-dependent conductivity model described by equation (2.1) the electrical conductivity of copper decreases as temperature increases. This relationship is clearly reflected in the simulation results. As shown in Figure 3.6, the temperature of the copper rises progressively along the flow direction from the inlet to the outlet. In contrast, Figure 3.7 displays an inverse trend: the electrical conductivity diminishes along the same path. The similarity in the spatial distribution of colors between the two plots, though with opposite gradients, confirms this inverse correlation and highlights the importance of thermal management in preserving favorable electrical properties within the conductor.

To provide accurate input for the subsequent electromagnetic simulation, the copper temperature was averaged over the entire copper volume. This volumetric average yields a representative mean temperature that is used to update the material's electrical conductivity accordingly, ensuring consistency between the thermal and electromagnetic simulations.

3 Electromagnetic simulation

3.1 Geometry

The stator windings are connected in a star configuration and their spatial distribution follows the star of slots rule. Figure 3.9 illustrates the physical arrangement of the windings within the stator and the interconnection pattern for a single electrical phase. The remaining two phases are connected in an analogous manner to form the complete three-phase system.

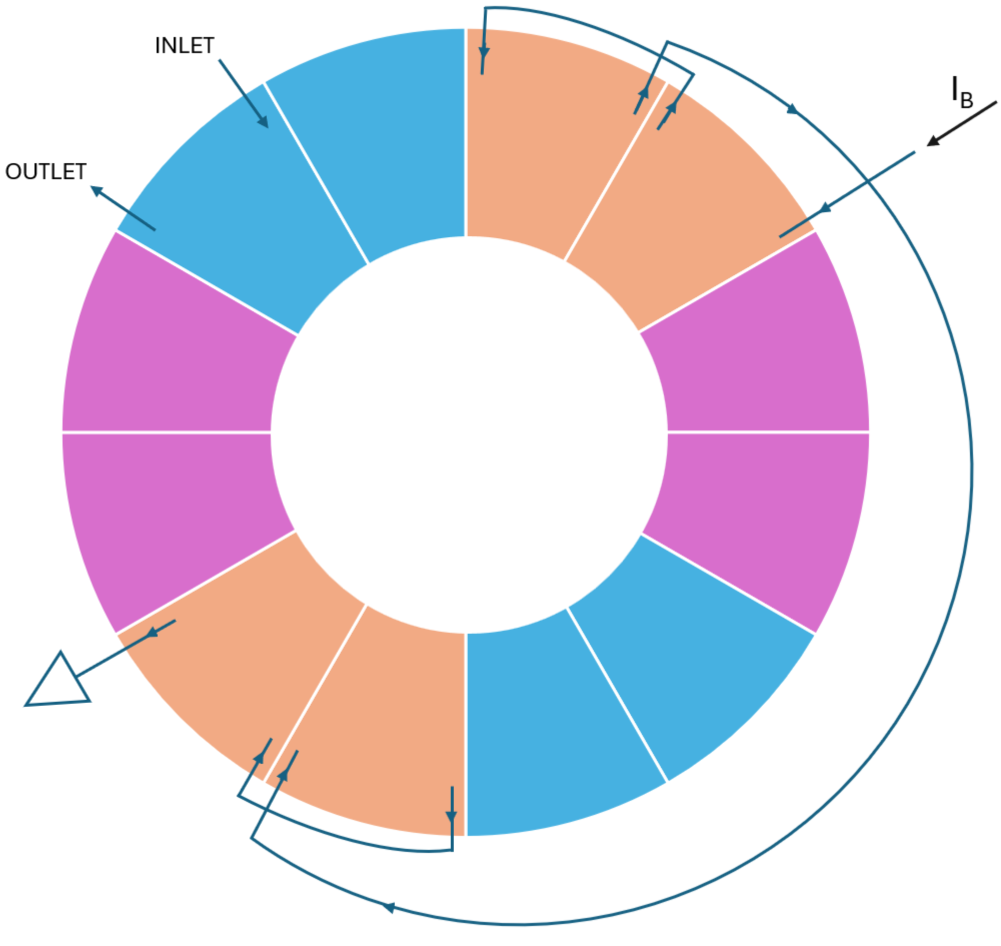

Figure 3.9: Coils position and connections

D_{ext}	310 $[mm]$	stator external diameter
D_{int}	150 $[mm]$	stator internal diameter
h_{coils}	19 $[mm]$	coil height
h_{teeth}	33 $[mm]$	teeth height
$h_{magnets}$	6 $[mm]$	magnets height
h_{iron}	15 $[mm]$	iron height

Table 3.4: Motor dimensions

In Figure 3.10, the actual geometry simulated in COMSOL is shown, along with the corresponding mesh applied to each domain. The mesh was designed to strike an appropriate balance between computational accuracy and simulation time, ensuring reliable results while maintaining efficiency in the numerical solution process.

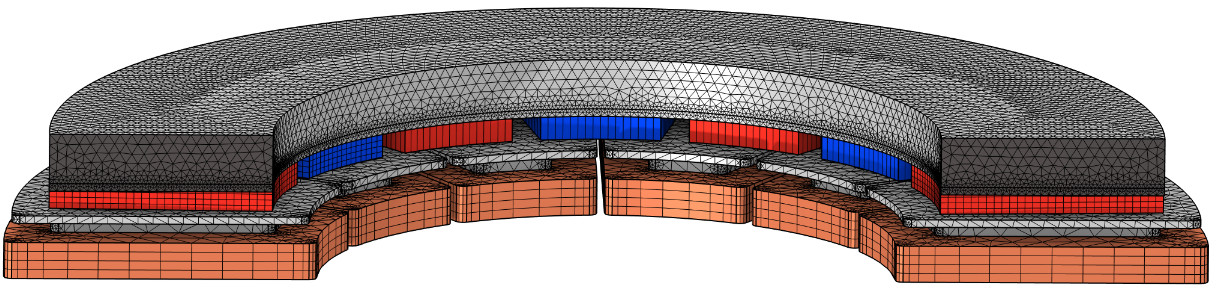

Figure 3.10: Simulation geometry and mesh used in COMSOL

3.2 Hollow windings

In the electromagnetic simulation the stator windings are not modeled with their full geometric detail. Instead, they are represented using the *Homogenized Multiturn* domain, a simplification that significantly reduces computational complexity while maintaining high accuracy in the evaluation of magnetic field distribution and torque production.

A homogenized multiturn coil is a mathematical abstraction used to model a bundle of turns as a single equivalent volumetric domain in which current density is distributed uniformly. Rather than explicitly resolving the geometry of each turn and the insulation gaps between them, the total coil volume is treated as a continuous conducting region. This volume is assigned a specified number of turns, a fill factor (previously calculated), and a defined coil conductivity. The result is a model that accurately captures the coil's electromagnetic behavior, including its magnetomotive force and spatial distribution, without the computational cost of meshing fine structural details.

To ensure the validity of the model, the dimensions of each homogenized coil domain are matched precisely to the external dimensions of the corresponding physical winding. The number of turns is set based on the coil configuration and the fill factor is defined to reflect the packing density of the copper within the insulating resin.

The excitation current is modeled as a sinusoidal waveform, applied in phase or anti-phase across the coils depending on their spatial distribution. The direction of current flow through each coil domain must be specified to correctly represent the winding pattern and magnetic field orientation. In COMSOL this is done by defining inlet terminal on the homogenized coil domain, which determines the resulting magnetic flux linkage.

Owing to the geometric symmetries discussed in previous sections, the simulation domain is reduced to a quarter of the full motor geometry. Specifically, only six homogenized coils are included, corresponding to half of the 12 coils in the complete stator, by exploiting mirror symmetry along the xy plane. Furthermore, the height of each coil domain is halved along the z-axis, taking advantage of axial symmetry.

This approach allows accurate modeling of the full machine behavior while minimizing the computational resources required.

3.3 Stator teeth

The stator teeth in the simulated machine are modeled using Somaloy® 700HR 5P [11], a soft magnetic composite (SMC) developed specifically for high-frequency and high-efficiency electromagnetic applications. Soft magnetic composites are isotropic, powder-based ferromagnetic materials where each particle is individually coated with an electrically insulating layer. These particles are compacted under high pressure and subsequently heat treated, producing components with low eddy current losses, even under rapid field variation.

Compared to traditional laminated steel, SMCs offer improved performance in 3D flux environments and reduce eddy current losses due to their granular structure and high electrical resistivity. In the case of Somaloy® 700HR 5P, the material is compacted at 800 MPa and heat treated in a nitrogen atmosphere at 650°C, resulting in a bulk resistivity of approximately 700 $[\mu\Omega \cdot m]$. This high resistivity significantly suppresses circulating eddy currents, making it ideal for applications involving fast magnetic field changes such as those encountered in axial flux topologies.

During operation, the stator teeth undergo continuous magnetization and demagnetization cycles, leading to magnetic core losses that must be accurately modeled. These losses are primarily composed of hysteresis and eddy current losses, and they are quantified in the simulation using the classical Steinmetz model (1.4). For Somaloy® 700HR 5P, the coefficients k, α, and β were obtained by interpolating the manufacturer's core loss data provided at multiple flux densities and frequencies.

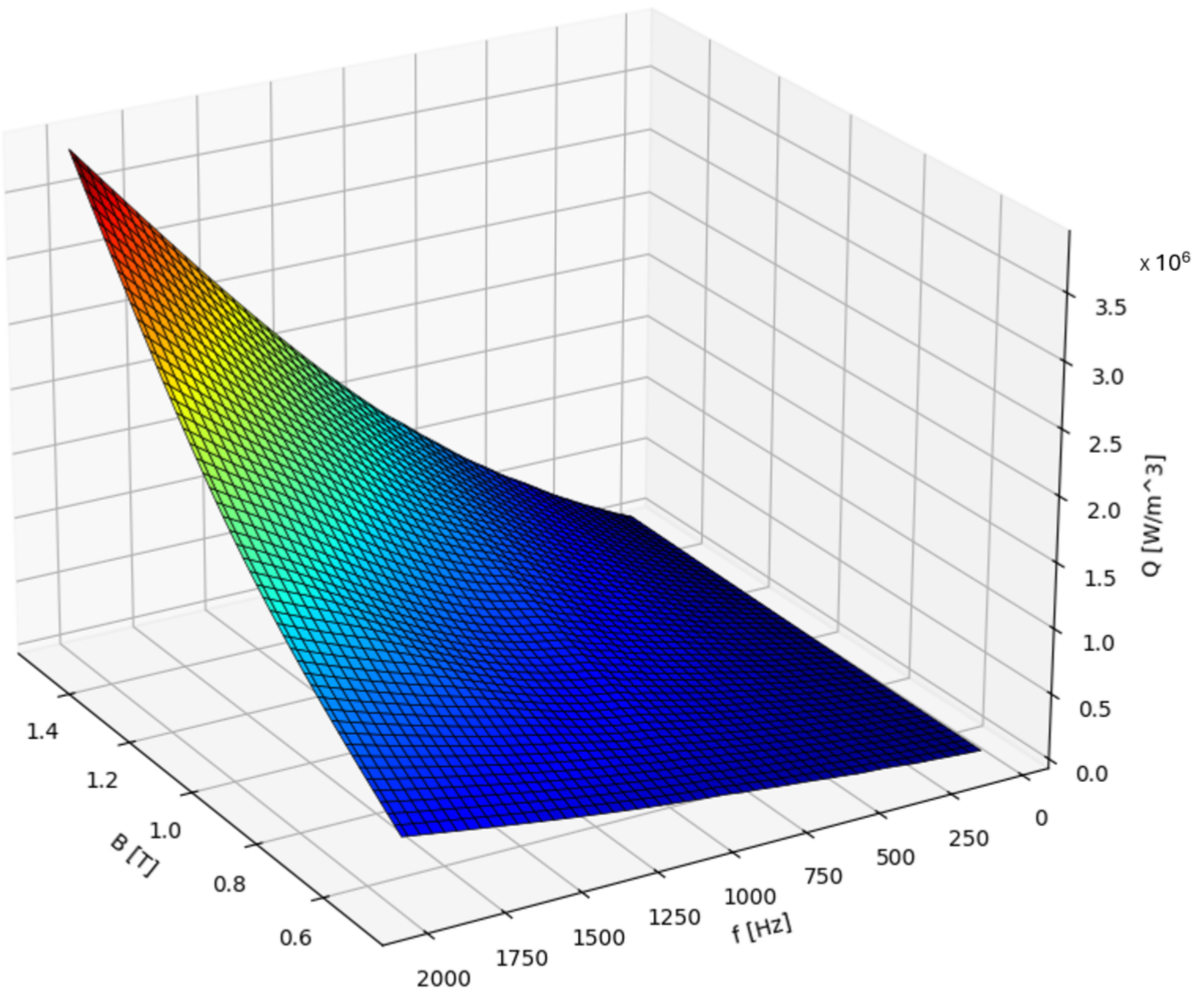

Figure 3.11: Somaloy® 700HR 5P losses surface

k	261.148
α	1.138
β	1.785

Table 3.5: k, α and β for Somaloy® 700HR 5P

In the simulations, the B–H magnetization curve of the material was implemented to represent the nonlinear magnetic behavior of the stator teeth. Figure 3.12 illustrates the first magnetization curve of the material, showing the relationship between magnetic field strength and flux density up to 2.47 T. This curve was integrated into the finite element model to ensure proper treatment of local saturation effects, which are particularly relevant in regions of concentrated magnetic flux.

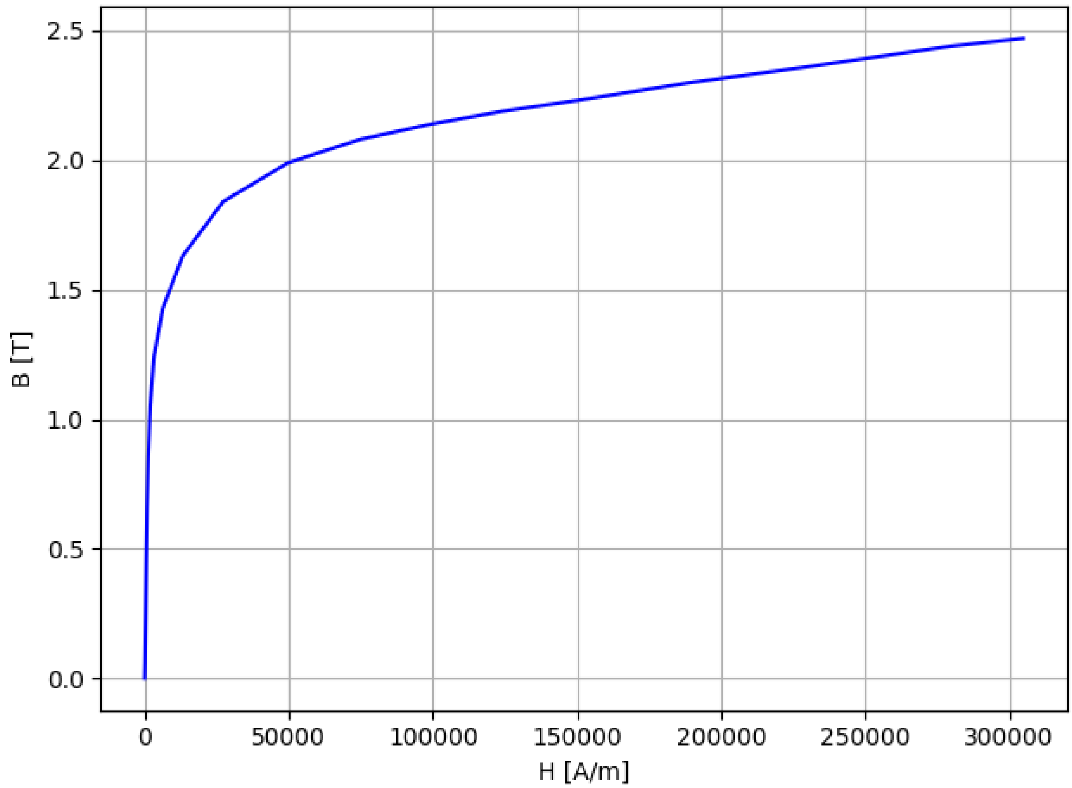

Figure 3.12: First magnetization curve of Somaloy® 700HR 5P

3.4 Permanent magnets

The role of permanent magnets is crucial in enabling high efficiency, high torque density, and compact machine design, however the performance of these magnets is inherently sensitive to temperature, and this must be carefully considered during both design and simulation phases.

When exposed to elevated temperatures, permanent magnets progressively lose their magnetization. This behavior is governed by two critical parameters: the *Curie temperature* (T_c) and the *demagnetizing field* (H). The Curie temperature is the threshold above which a ferromagnetic material loses its ability to maintain spontaneous magnetization due to thermal agitation overwhelming the alignment of magnetic domains. For the N45UH used in this work, the Curie temperature is approximately 310 °C, as specified in the manufacturer's datasheet [12].

Another important factor is the *demagnetization field*, which refers to the internal magnetic field opposing the magnet's own magnetization. When the operating point of the magnet falls below the so-called knee of the demagnetization curve, due to elevated temperature or external field perturbations, irreversible loss of magnetization may occur.

The permanent magnets selected for this axial flux motor are of type NdFeB, specifically the N45UH grade, produced by Arnold Magnetic Technologies [13]. These sintered neodymium-iron-boron magnets offer high magnetic performance at elevated temperatures, with high coercivity and residual flux density (B_r) nominally around 1.35 [T] at room temperature. The "UH" suffix indicates their suitability for high-temperature applications, with an operational limit of up to 180 °C without significant degradation.

A key characteristic of magnet performance is the temperature dependence of the remanent flux density. As temperature increases, the thermal agitation disrupts the alignment of magnetic domains, thereby reducing the effective B_r. This effect is quantified by the reversible temperature coefficient α_{B_r}, which for N45UH is approximately $-0.12[\%/°C]$ between 20 °C and 180 °C. The resulting decline in B_r with temperature is illustrated in Figure 3.13.

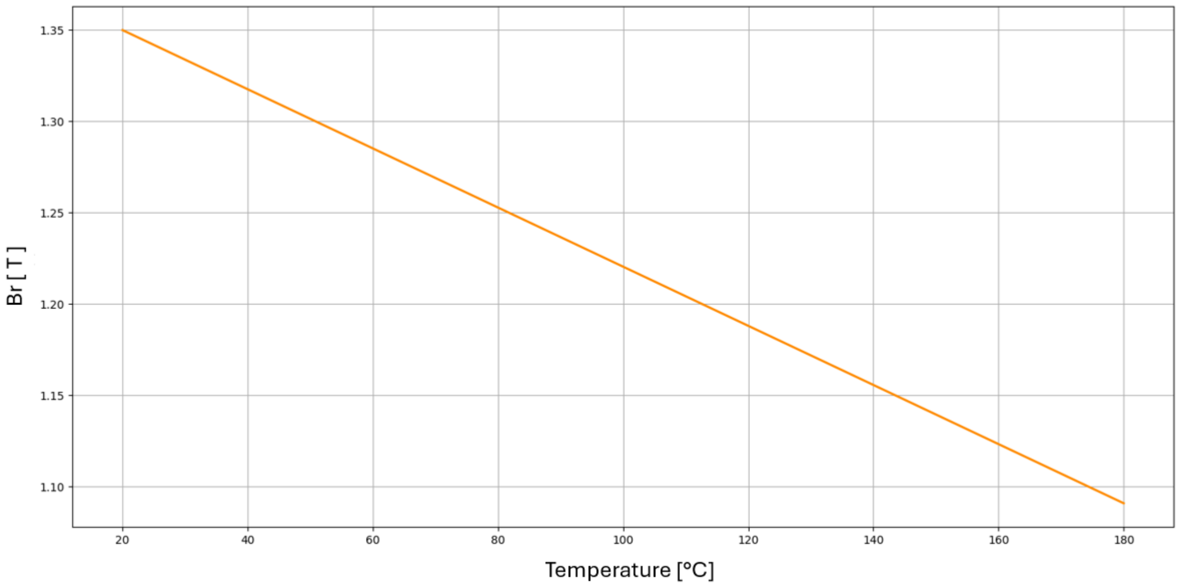

Figure 3.13: Remanent flux density vs. temperature for N45UH magnets

Understanding the thermal behavior of the magnets is essential in the design of electric machines, as it directly affects torque generation, efficiency, and demagnetization safety margins. The use of high-temperature NdFeB grades such as N45UH enables improved thermal robustness.

In the electromagnetic simulation, the operating temperature of the magnets is assumed equal to 90 [$°C$] based on thermal conditions within the motor. Consequently, the remanent flux density B_r is set equal to 1.2315 [T] according to the temperature dependence illustrated in Figure 3.13.

To evaluate the power losses occurring within the permanent magnets, the electrical resistivity of the N45UH material, provided in the manufacturer's datasheet, is assigned to the magnet domain. The simulation then solves for the time-varying electromagnetic fields and determines the eddy currents induced within the magnet volume. These circulating currents result in localized heating and are automatically integrated into the loss calculation by the solver, yielding an estimate of the total eddy current losses in the magnets under dynamic excitation.

3.5 Rotor Iron

As previously discussed, in axial flux machines the rotors are mechanically critical components, particularly in the double-rotor configuration where strong attractive forces between the opposing permanent magnets generate significant axial loads. These forces tend to induce bending in the rotor back iron, which, if not properly managed, can reduce the air gap and increase the risk of mechanical contact with the stator. Ensuring the mechanical integrity of the rotor under such conditions requires the use of a structural material with high stiffness, fatigue resistance, and dimensional stability.

To meet these mechanical requirements, the rotor was modeled using a high-strength structural alloy commonly employed in aerospace and power transmission systems. While this class of materials does not exhibit optimal magnetic or electrical characteristics, its mechanical robustness makes it a suitable choice for rotor back iron applications where rigidity is paramount.

In the electromagnetic simulations, magnetic losses within the rotor back iron are neglected. This simplification is justified by the fact that the magnetic flux in this region is largely dominated by the permanent magnets mounted on its surface. Consequently, the variation of magnetic flux density (B) inside the rotor structure is limited, and associated hysteresis losses are considered negligible compared to ohmic losses due to eddy currents.

To evaluate these ohmic losses, the electrical resistivity of the rotor material must be included in the model. A representative resistivity value for structural steels of this class is on the order of 5×10^{-7} $[\Omega \cdot m]$, which corresponds to a conductivity of approximately 2×10^{6} $[S/m]$. This value was adopted in the COMSOL simulations to estimate resistive losses due to induced eddy currents.

As described in Section 1.3, the skin effect causes eddy currents to concentrate near the surface of conductive materials. In the context of this motor, such currents are primarily confined to the inner surface of the rotor back iron, facing the stator, where time-varying magnetic fields are most intense. The skin depth at the operating frequencies of this motor is small, leading to localized current densities and power dissipation.

To resolve these effects accurately, a highly refined mesh was applied to the magnet-facing region of the rotor, with element edge lengths as small as 0.1 mm. This mesh granularity ensures accurate modeling of current density gradients and loss concentrations. In contrast, coarser meshing was applied to low-sensitivity regions of the rotor where eddy current effects are negligible, minimizing computational cost while preserving simulation fidelity.

3.6 Results

Ampere-turn (At)	2484 [A]
Electrical conductivity (σ_{CU})	59.2 [MS/m]
Remanent flux density (B_R)	1.2315 [T]
Coils losses (Pc)	2.2 [kW]
Magnets losses (Pm)	2.1 [kW]
Iron losses (Pi)	2.5 [kW]
Teeth losses (Pt)	0.6 [kW]
Torque (T_{AVG})	275.7 [Nm]
Torque ripple	9.3 [%]
Electrical power (P_{in})	76.7 [kW]
Mechanical power (P_{out})	69.3 [kW]
Efficiency	90.4 [%]

Table 3.6: Electromagnetic simulation results

The AC losses associated with skin and proximity effects, as discussed in Section 3.2, are not directly resolved by the electromagnetic simulation performed in COMSOL. In typical analyses, these losses are estimated analytically and subsequently incorporated into the overall loss budget. However, in the present case, their contribution can be considered negligible. According to the analytical expression for skin depth, given in Equation (1.3), the calculated skin depth in copper at the excitation frequency of interest is approximately 3.9 [mm]. This value is significantly greater than the wall thickness of the hollow winding, which measures only 0.9 [mm]. As a result, the current distribution across the conductor remains nearly uniform, and the influence of the skin effect is minimal. Consequently, AC losses within the stator windings can be justifiably neglected in this analysis.

The electromagnetic simulation yields the time-dependent flux linkage for each of the three phases, as shown in Figure 3.14. This total flux linkage, denoted λ, comprises two principal components: the contribution from the permanent magnets (λ_m), and the component induced by the stator currents flowing through the windings (λ_i).

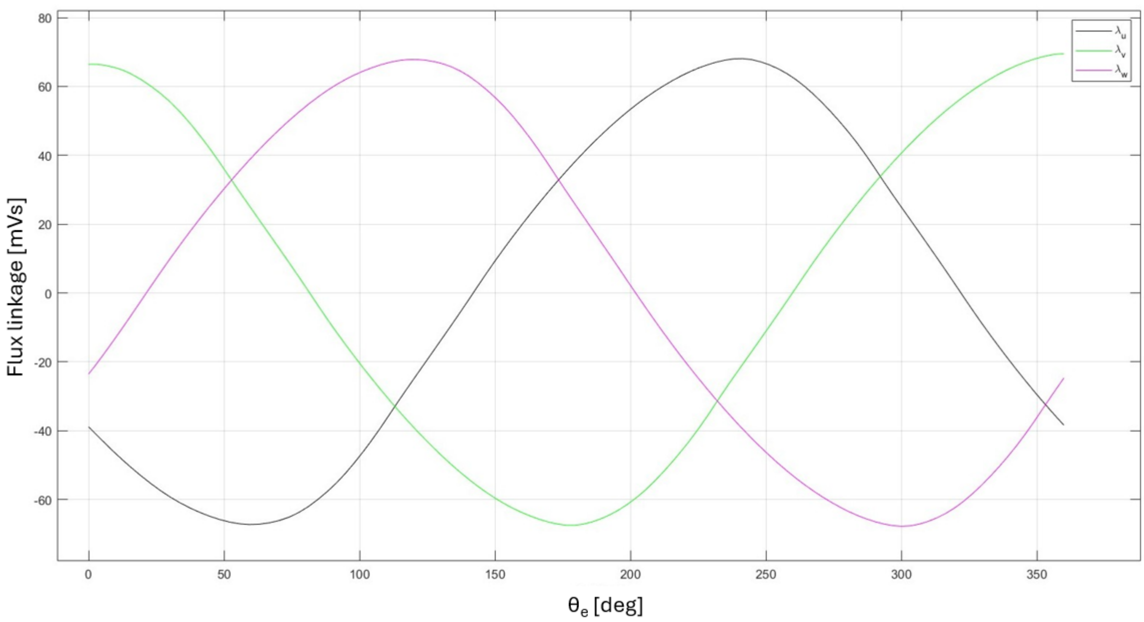

Figure 3.14: Flux linkage [mVs]

In accordance with Faraday's law (1.1) of electromagnetic induction, the voltage induced across each stator winding, commonly referred to as the back electromotive force, is given by the time derivative of the total flux linkage. By numerically differentiating the flux linkage signals, the phase voltages were reconstructed. The resulting voltage waveforms, which reflect the combined influence of permanent magnet excitation and current-induced fields, are presented in Figure 3.15.

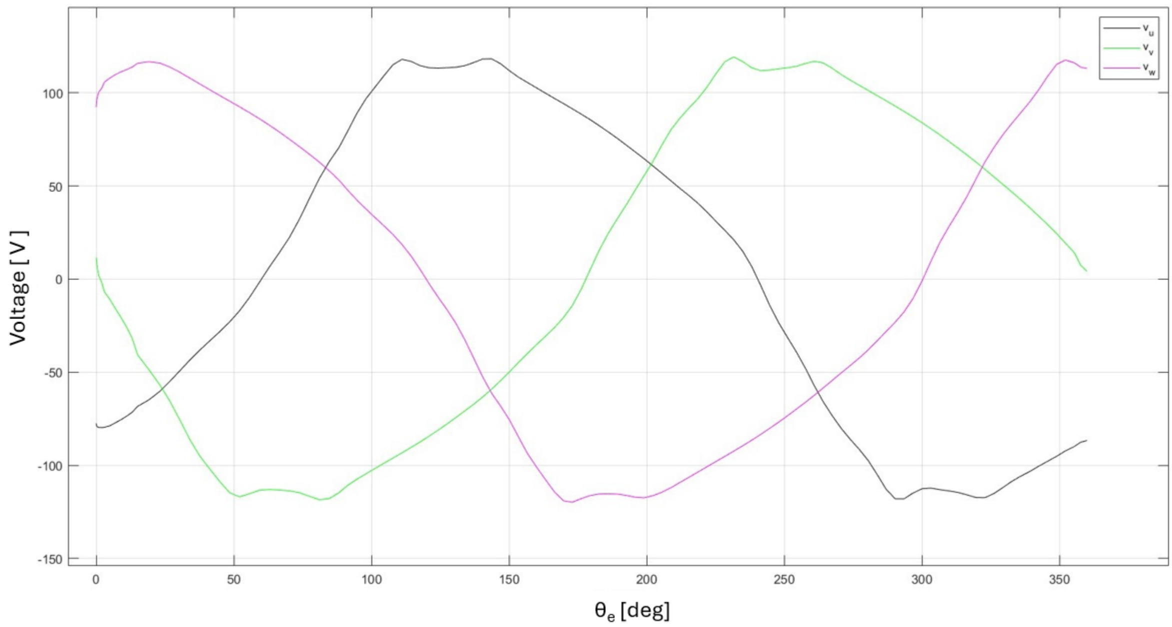

Figure 3.15: Voltage [V]

To isolate and quantify the contribution of the permanent magnets to the total flux linkage, a dedicated electromagnetic simulation was performed in which the stator current was set to zero while maintaining rotor motion. Although this operating condition is not physically realizable in practice, it is enabled by the simulation environment and provides valuable insights. In the absence of stator current, the resulting flux linkage arises only from the magnetic field generated by the permanent magnets, with no contribution from current-induced magnetic fields.

Once the phase flux linkage waveforms were obtained, the Park transformation was applied. This mathematical transformation projects the three-phase flux linkage components onto a rotating reference frame that is fixed to the rotor position. It allows the representation of the system using only two orthogonal components: the direct axis (d) and quadrature axis (q).

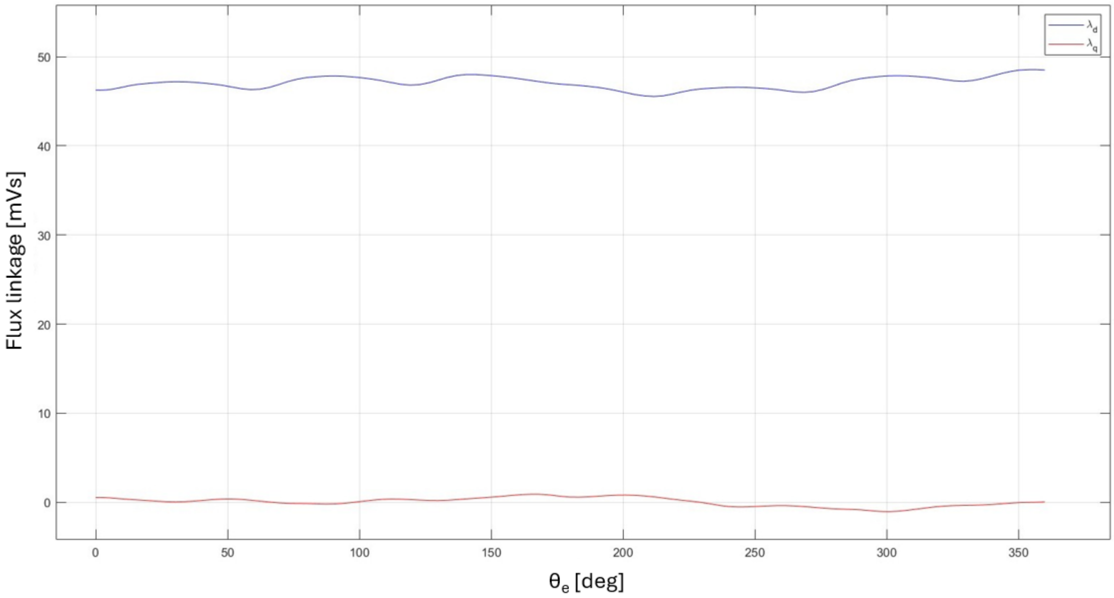

Figure 3.16: No load flux linkage in dq reference frame

As shown in Figure 3.16, the result is consistent with the expected behavior of SPM machines: the q-axis flux linkage λ_q is approximately zero, while the d-axis flux linkage λ_d reaches a maximum value. In this case, λ_d represents the magnetically induced flux linkage λ_m, and its magnitude is found to be approximately 47 $[mVs]$.

Furthermore, when the Park transformation is applied to the three-phase stator currents under normal operating conditions (with sinusoidal balanced excitation), the d-axis current component i_d is zero, while the q-axis current component i_q reaches a peak value of $585[A]$.

With these values, the maximum electromagnetic torque can be estimated analytically using the standard torque equation for SPM machines:

$$T_{\max} = \frac{3}{2} \cdot p \cdot \lambda_m \cdot i_q$$

where p is the number of pole pairs. For the studied motor, this yields a torque of approximately 288.7 $[Nm]$, which is in excellent agreement with the torque obtained from the electromagnetic simulation in COMSOL. This consistency validates both the simulation framework and the analytical assumptions.

An electromagnetic simulation was performed by sweeping the RMS value of the stator current in order to evaluate the torque response under increasing load conditions. As expected, the resulting plot shown in Figure 3.17 reveals that the torque does not increase linearly with current across the entire range. Instead, the curve exhibits noticeable deviation from linearity at higher current levels due to magnetic saturation effects in the ferromagnetic components of the motor.

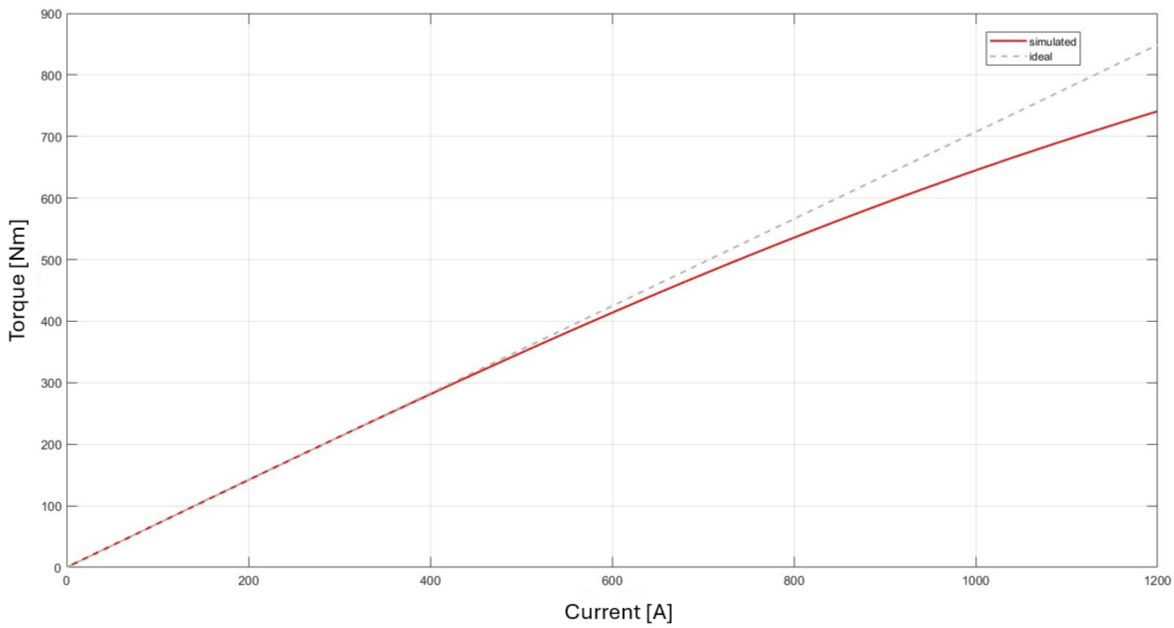

Figure 3.17: Torque VS input current

A dashed grey line is included in the plot to represent the ideal linear trend that would occur in the absence of saturation, while the red curve reflects the actual torque values obtained from simulation. The onset of saturation is observed at approximately 500 [A], indicating that when operating at the nominal current of 414 [A], the motor remains within the quasi-linear region of operation. This behavior confirms the effectiveness of the magnetic design and suggests that the internal components have been appropriately dimensioned to ensure high performance without premature saturation.

3.7 Hollow windings realization

Although the coil shown in Figure 3.18 is not the specific design studied in this thesis, it serves as tangible evidence of the current manufacturability of hollow stator windings using pure copper additive manufacturing. This example demonstrates the feasibility of producing complex internal geometries, such as embedded cooling channels, which are otherwise difficult or impossible to achieve using conventional subtractive methods. The successful realization of this geometry demonstrates the growing maturity and industrial viability of pure copper additive manufacturing technologies, and supports the underlying motivation of this research: to explore the integration of these coils into high-performance electric machines.

Figure 3.18: Hollow copper winding produced via additive manufacturing

Source: AddToShape srl

4. Conclusions

This thesis has explored the performance potential achievable by combining two advanced and emerging technologies in the field of electric machines: axial flux motor topologies and pure copper additive manufacturing. The study specifically focused on the integration of internally cooled stator windings, enabled by additive manufacturing, within a yokeless double-rotor axial flux motor architecture. The concept of embedding hollow stator coils with internal channels offers a promising route toward improved thermal management in high-performance electric drives. By extracting heat directly from the windings, the primary source of Joule losses, the design enables more effective and localized thermal dissipation, thus mitigating overheating risks and enabling higher current densities.

However, this design innovation also introduces specific trade-offs. The inclusion of internal cooling ducts within the windings reduces the available space for copper conductors, which in turn limits the number of turns that can be accommodated within each slot. Since the induced voltage in each phase is directly proportional to the flux linkage, and the flux linkage itself scales with the number of turns, this geometric constraint results in a significantly reduced phase voltage. In practical applications, where the total electrical power must remain constant, a lower phase voltage implies the need for a proportionally higher phase current to maintain the same power output. However, inverters used for motor drive applications are typically constrained in the maximum current they can safely deliver, due to both thermal limitations and the physical design of their power electronic components. As a result, the ability to increase current to compensate for the reduced voltage is inherently limited.

Moreover, even though internal cooling allows for better thermal handling, the current density in the copper does not necessarily increase proportionally. This is because the hollow nature of the conductors requires a significantly larger cross-sectional area to accommodate the internal coolant channels. Unlike traditional flat conductors or wires, which are optimized for compactness, the hollow geometry introduces geometric overhead. As a consequence, the larger conductor volume spreads the current over a wider area, reducing the effective current density and partially offsetting the thermal advantage. This current limitation, both from the inverter and the physical conductor geometry, imposes a constraint on the maximum electrical power that can be delivered to the motor. Consequently, even if the motor is thermally capable of handling higher currents, thanks to the enhanced internal cooling of the hollow coils, the overall torque output becomes limited by the current delivery capabilities of the inverter and the current density limits imposed by the conductor geometry.

This observation suggests that the adoption of hollow conductors can only be fully justified when coupled with a power electronics system that is capable of delivering higher currents at lower voltages. In other words, the system must be co-designed to exploit the thermal and structural advantages of hollow coil technology while mitigating its inherent electromagnetic penalties. A high-current, low-voltage inverter allows for greater exploitation of the enhanced cooling capacity, enabling operation at higher current densities without exceeding thermal limits, and thereby recovering the torque losses otherwise induced by the reduced number of turns. In summary, while hollow coils manufactured via pure copper additive processes present undeniable benefits in terms of thermal performance and compactness, their successful application in electric machines requires careful integration with matching inverter technologies. Only through a holistic co-design approach, simultaneously addressing thermal, electromagnetic, and power electronics domains, can the full potential of this innovative winding concept be realized.

Bibliography

[1] Richard Phillips and Tim Woolmer. "AC Copper Losses in Edge-Wound Coils in a YASA Motor". In: *IEEE International Electric Machines & Drives Conference (IEMDC)*. IEEE. 2020. URL: https://ieeexplore.ieee.org/document/9545356.

[2] Charles P. Steinmetz. "On the Law of Hysteresis". In: *Proceedings of the IEEE* 72.2 (1984), pp. 197–221.

[3] G. Bertotti. "General Properties of Power Losses in Soft Ferromagnetic Materials". In: *IEEE Transactions on Magnetics* 24.1 (1988), pp. 621–630.

[4] H.M. Pan. "Advanced Materials in 3D/4D Printing Technology". In: *Polymers* 14 (2022). URL: https://doi.org/10.3390/polym14163255.

[5] *ISO/ASTM 52900:2021 - Additive manufacturing — General principles — Fundamentals and vocabulary*. International Organization for Standardization and ASTM International, 2021.

[6] N.D. Dejene and H.G. Lemu. "Current Status and Challenges of Powder Bed Fusion-Based Metal Additive Manufacturing: Literature Review". In: *Metals* 13 (2023). URL: https://doi.org/10.3390/met13020424.

[7] Y. Zhou et al. "The Processing Map of Laser Powder Bed Fusion In-Situ Alloying for Controlling the Composition Inhomogeneity of AlCu Alloy". In: *Metals* 13.1 (2023). URL: https://doi.org/10.3390/met13010097.

[8] Giuliano Cammarata. *Trasmissione del Calore [Heat Transfer]*. Dispensa didattica [Teaching material]. Università degli Studi di Catania, 2016.

[9] *EOS M 290 1kW – Technical Data Sheet*. EOS GmbH Electro Optical Systems. Robert-Stirling-Ring 1, 82152 Krailling / Munich, Germany, 2025. URL: https://www.eos.info.

[10] C. Ricca A. Di Gerlando G. Foglia. "Design of a High Torque Density In-Wheel YASA AFPM Motor". In: Politecnico di Milano. URL: https://re.public.polimi.it/bitstream/11311/1160482/1/tmp-2985-000027.pdf.

[11] Höganäs AB. *Somaloy 700HR 5P, high performance soft magnetic composite for press and sinter applications*. https://www.hoganas.com/globalassets/downloads/libary/somaloy_somaloy-5p-material-data_2274hog.pdf. Höganäs AB, 2025.

[12] Arnold Magnetic Technologies. *N45UH, Sintered Neodymium-Iron-Boron Magnets, Technical Datasheet*. https://www.arnoldmagnetics.com. Rev. 210607. 770 Linden Avenue, Rochester, NY 14625, USA: Arnold Magnetic Technologies Corp.

[13] John J. Croat and John Ormerod. "Fundamental Properties of Permanent Magnets". In: *Modern Permanent Magnets*. Woodhead Publishing, Elsevier Ltd., 2022. Chap. 2.